Bulletin of the Seismological Society of America, Vol. 75, No. 4, pp. 965–1004, August 1985

TELESEISMIC TIME FUNCTIONS FOR LARGE, SHALLOW SUBDUCTION ZONE EARTHQUAKES

By Stephen H. Hartzell and Thomas H. Heaton

Abstract

Broadband vertical *P*-wave records are analyzed from 63 of the largest shallow subduction zone earthquakes which have occurred in the circum-Pacific in the last 45 yr. Most of the records studied come from a common instrument, the Pasadena, California, Benioff 1–90 seismometer. Propagation and instrument effects are deconvolved from the *P*-wave records using a damped least-squares inversion to obtain the teleseismic source time function. The inversion has the additional constraint that the time function be positive everywhere. The period band over which the time functions are considered reliable is from 2.5 to 50 sec. Fourier displacement amplitude spectra computed for each of the 1–90 *P*-wave trains indicate spectral slopes measured between 2 and 50 sec of $\omega^{-1.0}$ to $\omega^{-2.25}$ with an average value of $\omega^{-1.5}$. These values assume an average attenuation of $t^* = 1.0$. The seismic moments derived from the *P*-wave time functions compare well with other published values for earthquakes having moments smaller than 2.5×10^{28} dyne-cm ($M_w = 8.2$). Because the 1–90 seismometer has little response at very long periods, this technique underestimates the moments of the very largest events. The time functions are characterized using five parameters: (1) spectral slope between 2 and 50 sec; (2) roughness of the time function; (3) multiplicity of sources; (4) pulse widths of individual sources; and (5) overall signal duration. The 63 earthquakes studied come from 15 subduction zones with a wide range in the ages of subducted lithosphere, convergence rates, and maximum size of earthquakes. Comparing the time function parameters with age, rate, and M_w of the subduction zone does not yield obvious global trends. However, most of the subduction zones do behave characteristically and can be grouped accordingly.

Introduction

In terms of the details of fault rupture or source complexity, our knowledge of the very largest earthquakes is limited. Until very recently, most of what was known about major earthquakes consisted of estimates of their focal mechanism and moment. Although this information is of fundamental interest, it is desirable to know more about the spatial and temporal distribution of moment release. The very largest earthquakes have been shallow thrust events at convergent plate boundaries. In this paper, we present the results of a survey study of teleseismic source time functions for major shallow thrust earthquakes. Sixty-three of the largest shallow subduction zone earthquakes that have occurred in the circum-Pacific in the last 45 yr are studied. Earthquakes from 15 different subduction zones with very different ages of subducted lithosphere and plate convergence rates are included.

The source complexity of the earthquakes is appraised by the physical features of the teleseismic source time functions. These features include the overall duration, multiple or single event character, individual source pulse widths, and roughness of the time function. The above measures of source size and complexity can then be compared with the age of subducted lithosphere, plate convergence rate, and other physical parameters of the subduction zone. Such comparisons are important for increasing our understanding of the worldwide distribution of the largest earth-

quakes and their radiated energy. The teleseismic source time function gives information about source complexity which can be used in the estimation of strong ground motions. Studies of source complexity are also important to evaluate the validity of recent asperity models of faulting, where the fault is characterized by localized regions of higher strength. In subduction zone regimes, the maximum earthquake magnitude has been related to asperity size and to the mechanical coupling between the plates (Uyeda and Kanamori, 1979; Ruff and Kanamori, 1980, 1983; Lay *et al.*, 1982). The earthquake time functions in this paper will, we hope, add insight to these interpretations.

For the period range of interest, about 1 to 60 sec, *P*-wave radiation is the natural choice for study of source complexity. It is useful for later discussion to briefly review the most common techniques which have been used to estimate teleseismic body-wave, source time functions. The techniques can be grouped into two general types: (1) division of the record by the theoretical point impulse response in the frequency domain; and (2) parameterization of the time function. With the second approach, the optimum values of the parameters are obtained by various methods including cross-correlation, linear least-squares, and maximum likelihood. Boatwright (1980) utilizes a direct deconvolution approach. The source time function is obtained by a recursive deconvolution in the time domain of the seismogram by a bandpass-filtered theoretical impulse response of the earth. The effect of the filtering on the low-frequency baseline of the time function is approximately removed by subtracting the effect of the same processing performed on an idealized functional form of the seismogram. Source finiteness is neglected. Burdick and Mellman (1976) invert *P* waveforms from WWSSN stations for the 1968 Borrego Mountain earthquake. In their approach, the source time function is parameterized by a few variables whose optimum values are obtained by a numerical correlation between the synthetics and the observations. Care should be exercised in applying such a technique, since the time function can only reflect that amount of complexity that is allowed for by the particular parameterization used. Kanamori and Stewart (1978) and Stewart and Kanamori (1982) use a forward modeling procedure to examine the complexity of WWSSN *P* waveforms. In their technique, a single point source, having a trapezoidal far-field time function, is chosen such that it simulates the very beginning of the *P* wave train. The synthetic for this point source is then subtracted from the observations. This process is repeated using the remaining waveform until all significant arrivals are accounted for. Depending on the complexity of the waveforms, this procedure can be quite tedious.

Kikuchi and Kanamori (1982) extend the method of Kanamori and Stewart (1978) so that complex body waves can be formally inverted for the source time function. The synthetic seismogram for an initial source with a ramp dislocation function, rise time τ, and rupture duration T is subtracted from the observations. The strength and arrival time of this source are determined by cross-correlation of the synthetic and data records. The process is continued for N iterations until an acceptable fit, measured in a least-squares sense, is obtained to the data. The best value of τ is obtained by trial and error. A linear baseline trend, which is a result of the band-limited nature of the data, is removed from the source time function. For multiple-station data, the relative timing of sources between stations can be used to locate each source with respect to a given hypocenter. Ruff and Kanamori (1983) estimate the source time function for several great earthquakes by solving the least-squares problem $[\boldsymbol{A}/\lambda \boldsymbol{I}]\boldsymbol{X} \simeq [\boldsymbol{b}/0]$. Here, $\boldsymbol{A}$ is a matrix of phase shifted Green's functions for the earth with narrow source time histories, $\boldsymbol{I}$ is the identity matrix,

λ is a damping or moment minimization parameter, $\boldsymbol{X}$ is the discretized source time function, and $\boldsymbol{b}$ is the observation vector. A long-period, half-sine function is added to the time function to shift the baseline. This adjustment is done to approximately compensate for the band-limited nature of the data and to obtain a mostly positive time function. Nabelek (1984a, b) parameterizes the teleseismic source time function either as a series of overlapping isosceles triangles for a point source, or overlapping trapezoids for a line source. The number of elementary sources, N, the rise time of each source, τ, and the duration of each source as seen at different azimuths (for the line source problem) are all set *a priori*. An iterative maximum likelihood inverse is used to find the best-fitting weight to be applied to each of the N sources.

All of the above techniques share the common limitations of the bandwidth of the data and the accuracy of the computed impulse response of the earth for the earthquake mechanism.

Data Set

Rather than study a few earthquakes in detail, we considered a survey study of a larger number of events in order to characterize the overall nature of shallow subduction zone earthquakes. The objective is to compare as many earthquakes of this type as possible by using body-wave records that have all been recorded on the same instrument. Although the full effect of the receiver structure may not be known, by using a common site and instrument, comparison studies between earthquakes are possible. The determination of the spatial and temporal rupture history of a three-dimensional source requires good azimuthal coverage of the radiated energy. In this study, only one station is used. Therefore, we obtain an estimate of the teleseismic source time function as viewed from one particular azimuth.

The desirable characteristics of the recording instrument for this study are: (1) a long time period of continuous operation; (2) a well-calibrated, broadband frequency response; and (3) a location such that most of the circum-Pacific lies at a distance between 30° and 90°, the distance range where direct P waves bottom in the lower mantle. The first two requirements rule out WWSSN stations. The instruments which do the best job of meeting the above requirements are the southern California array of Benioff 1–90 seismometers operated by the California Institute of Technology. These instruments have a 1-sec natural period seismometer, a 90-sec natural period galvanometer, and a peak gain of 3000 at 1 sec. Benioff 1–90 seismometers have operated at four sites in southern California: Pasadena; Riverside; Barrett; and Tinemaha. The Pasadena instrument was chosen because of its longer period of operation and because the records are free from obvious site reverberations. In a few cases, when Pasadena records could not be found, the Barrett record is used. The Barrett station writes seismograms very similar to those of the Pasadena station. On-scale records are available for almost every large, shallow subduction zone earthquake that has occurred since 1938. One notable exception is the 1964 Alaska earthquake. For completeness, we have substituted the Pasadena Wood-Anderson torsion seismometer record for the 1964 Alaska earthquake. Besides the 1964 Alaska event, the only other gap in the data set is for earthquakes in Mexico. These events are less than 30° from Pasadena and have been omitted to avoid upper mantle triplications.

The locations of the earthquakes studied are given in Figure 1 and Table 1. In total, 63 events are analyzed. In Figure 1 and Table 1 a numbering scheme is adopted for identification of the events and is used throughout this paper. The data

have been processed as follows. The vertical component of the Benioff 1–90 instrument is first digitized and bandpass-filtered from 1 to 60 sec using a double-pass zero phase Butterworth filter (Oppenheim and Schafer, 1975). The filtering is done to remove long- and short-period noise, primarily from digitizing. The records are then interpolated to a uniform time step of 0.2 sec. This time spacing gives a Nyquist frequency of 2.5 Hz, which is more than sufficient for the following analysis. The effects of the earth's structure, attenuation, and the instrument response are removed in the inversion process described below.

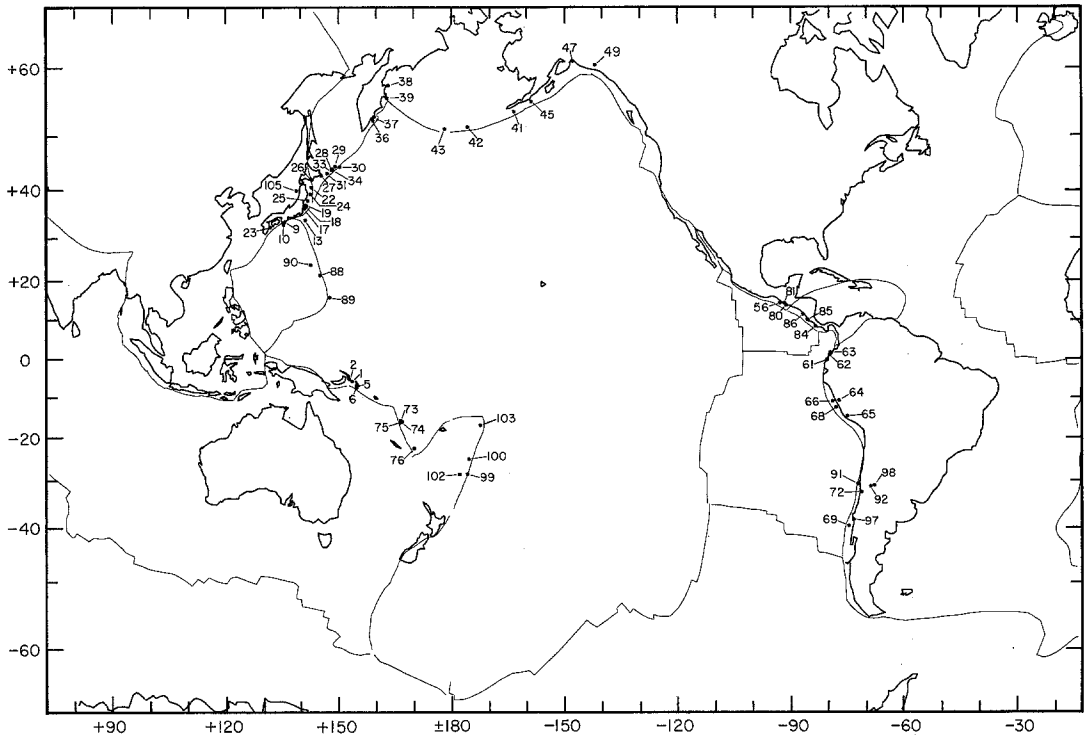

FIG. 1. Locations of the large shallow subduction zone earthquakes studied and the event numbers which they have been assigned. Light lines mark major crustal plate boundaries.

INVERSION METHOD

We now describe what we mean by the teleseismic P-wave time function and how we can calculate it from the observed P-wave train. Consider the fault shown in Figure 2, where the x coordinate runs along the fault strike, z is depth, and δ is the fault dip. If the dislocation rake angle is constant everywhere on the fault surface, then a single component of the teleseismically observed ground motion can be written as

$$U(t) = \int_{z_1}^{z_l} \int_0^L \dot{D}(x, z, t) * G(x, z, t) \frac{1}{\sin \delta} \, dx \, dz, \tag{1}$$

where z_1 and z_l are the top and bottom depths of the fault, L is the fault length, $G(x, z, t)$ is the earth's impulse response for each point on the fault, and $\cdot$ and $*$ denote time differentiation and convolution operators, respectively. $D(x, z, t)$ is the

TABLE 1

EARTHQUAKE PARAMETERS

Event No.	Latitude	Longitude	Depths (km)	Strike	Dip	Rake	Distance	Azimuth	Reference
1	5.5S	153.9E	27/34/41/48	345	45	90	91.4	56.0	1
2	4.9S	153.2E	22/29/36/43	240	40	55	91.6	56.0	1
5	6.6S	155.1E	17/24/31/38	306	36	90	91.0	55.9	1
6	7.1S	155.2E	15/22/29/36	303	40	90	91.2	55.9	1
9	33.7N	136.05E	17/24/31/38	216	10	90	83.1	53.5	2
10	33.13N	135.84E	17/24/31/38	220	10	90	83.6	53.3	2
13	34.1N	141.6E	35/42/49/56	135	70	−135	79.1	56.2	3
17	36.58N	141.34E	27/34/41/48	210 (200)	15 (10)	92	77.9	56.5	4
18	36.97N	141.71E	17/24/31/38	200	15 (10)	91	77.5	56.7	4
19	37.24N	141.75E	33/40/47/54	200	15 (10)	93	77.3	56.8	4
22	40.8N	143.2E	9/16/23/30	156	20	37	74.4	58.3	5
23	32.54N	132.3E	17/24/31/38	207	17	90	86.3	51.5	6
24	39.47N	142.9E	5/12/19/26	151	30	29	75.3	57.9	7
25	38.15N	142.2E	15/22/29/36	190	20	76	76.5	57.2	8
26	42.5N	143E	9/16/23/30	220	20	90	73.6	58.6	9
27	43.05N	145.8E	35/42/49/56	230	27	112	71.6	60.3	10
28	44.38N	148.58E	22/29/36/43	225	30	90	69.1	62.4	11
29	44.8N	149.5E	40/47/54/61	223	22	90	68.4	63.0	12
30	44.7N	150.7E	15/22/29/36	225	10	90	67.7	63.7	13
31	43.5N	147.4E	17/24/31/38	220	16	90	70.3	61.4	14
33	44.2N	148.8E	22/29/36/43	213	20	88	69.1	62.4	15
34	44.1N	148.6E	44/51/58/65	195	26	51	69.3	62.3	15
36	52.6N	159.5E	15/22/29/36	214	30	110	59.3	72.8	16
37	53.2N	159.8E	54/61/68/75	225	10	90	59.0	73.4	17*
38	57.8N	163.6E	17/24/31/38	225	16	92	55.8	79.1	18
39	56.0N	163.3E	17/24/31/38	225	10 (18)	90	56.3	77.6	18
41	54.0N	163.0W	17/24/31/38	287	70	−90	37.0	103.9	19
42	51.6N	175.4W	17/24/31/38	260	18	90	44.2	90.2	20*
43	51.3N	178.6E	27/34/41/48	289	18	137.7	48.0	85.3	21
45	55.5N	158.4W	27/34/41/48	260	10	90	34.9	110.7	22*
47	61.0N	147.5W	9/16/23/30	246	20	90	32.8	131.4	23
49	60.5N	141.5W	5/12/19/26	250	12	90	30.4	139.5	24
56	14.5N	92.6W	15/22/29/36	296	20	90	30.3	−45.2	25
61	0.01S	80.1W	17/24/31/38	31	20	126	49.2	−42.4	26*
62	1.2N	79.4W	17/24/31/38	31	20	126	48.8	−43.6	26*
63	1.9N	79.3W	17/24/31/38	31	20	126	48.4	−44.1	26
64	10.5S	77.0W	15/22/29/36	340	15	90	59.1	−39.5	27*
65	14.5S	74.8W	15/22/29/36	340	15	90	63.6	−39.5	27*
66	10.7S	78.7W	22/29/36/43	335 (330)	12	90	58.2	−38.3	27
68	12.26S	77.8W	5/12/19/26	340	17	90	60.0	−38.3	28
69	39.5S	74.5W	22/29/36/43	10	10	90	83.6	−35.1	29
72	32.5S	71.1W	27/34/41/48	15	24	93	79.7	−38.1	30
73	15.5S	166.9E	15/22/29/36	330	45	100	86.6	53.3	31
74	15.8S	167.2E	15/22/29/36	334	35	90	86.5	53.2	31
75	16S	166.8E	17/24/31/38	334	10	90	87.0	53.3	31
76	22.3S	170.4E	5/12/19/26	322	25	90	88.1	51.8	32
80	14N	91W	17/24/31/38	296	15	80	31.7	−46.0	33*
81	14.5N	91.5W	17/24/31/38	296	15	80	31.0	−46.2	33*
84	8.67N	83.16W	17/24/31/38	308	20	90	40.9	−46.5	34*
85	10.3N	85.2W	17/24/31/38	308	20	90	38.3	−46.6	34*
86	11.7N	86.5W	17/24/31/38	308	20	90	36.5	−47.0	34*
88	21.5N	145.5E	17/24/31/38	160	20	90	83.2	56.1	35*
89	16.0N	148.0E	17/24/31/38	160	20	90	84.3	56.2	35*
90	24.0N	143.0E	17/24/31/38	160	20	90	83.7	55.5	35*
91	30.7S	72.0W	17/24/31/38	20	25	110	77.8	−37.7	36*
92	31.2S	68.7W	17/24/31/38	20	25	110	80.0	−39.8	36*

TABLE 1—*Continued*

Event No.	Latitude	Longitude	Depths (km)	Strike	Dip	Rake	Distance	Azimuth	Reference
97	38.2S	73.2W	5/12/19/26	20	20	110	83.2	−36.1	36*
98	31.0S	67.7W	5/12/19/26	20	20	110	80.4	−40.4	36*
99	28.3S	175.5W	17/24/31/38	200	15	90	82.5	44.8	37*
100	24.9S	175.1W	5/12/19/26	200	20	90	79.8	44.9	37*
102	28.4S	177.6W	17/24/31/38	200	15	90	83.9	45.9	37*
103	16.7S	172.1W	17/24/31/38	200	15	90	72.0	44.8	37*
105	40.2N	139.2E	17/24/31/38	15	30	104	77.3	56.0	38

* Mechanism estimated from trench orientation.

The references used are: 1, Lay and Kanamori (1980); 2, Kanamori (1972a); 3, Ichikawa (1971); 4, Abe (1977); 5, Kanamori (1971); 6, Shiono *et al.* (1980); 7, Yoshioka and Abe (1976); 8, Seno *et al.* (1980); 9, Kasahara (1975); 10, Shimazaki (1974); 11, Fukao and Furumoto (1979); 12, Kanamori (1970a); 13, Fukao (1979); 14, Abe (1973); 15, Regan and Kanamori (1980); 16, Kanamori (1976); 17, Seno and Eguchi (1983); 18, Cormier (1975); 19, Kanamori (1972b); 20, Sykes (1971); 21, Wu and Kanamori (1973); 22, Davies *et al.* (1981); 23, Kanamori (1970b); 24, Boatwright (1980); 25, Chael and Stewart (1982); 26, Kanamori and Given (1981); 27, Abe (1972); 28, Stewart, G. (personal communication, 1984); 29, Kanamori and Cipar (1974); 30, Malgrange *et al.* (1981); 31, Ebel (1980); 32, Vidale and Kanamori (1983); 33, McNally and Minster (1981); 34, Kelleher *et al.* (1973); 35, Katsumata and Sykes (1969); 36, Stauder (1973); 37, Isacks, *et al.* (1969); 38, Kanamori and Astiz (1984).

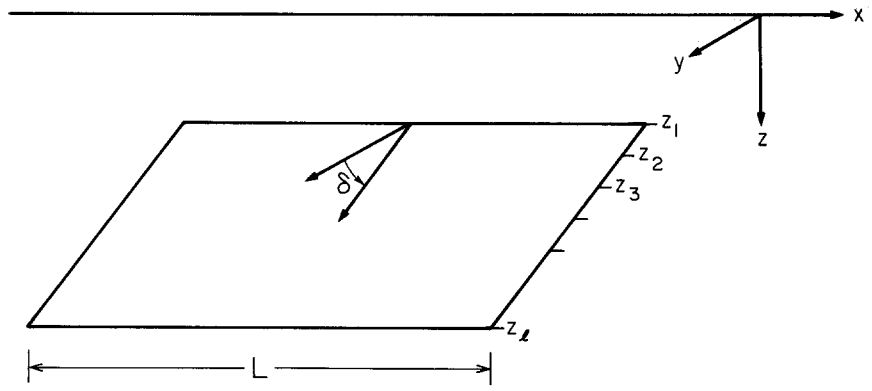

FIG. 2. Fault plane model.

dislocation time history for each point on the fault and includes the effects of rupture velocity or any other rupture complexities.

For a source viewed at teleseismic distances, small changes in distance mainly introduce a timing shift to the impulse response, and thus

$$G(x, z, t) \simeq G(x_0, z, t) * \delta(t - T(x)), \tag{2}$$

where $\delta(t)$ is a Dirac delta function, x_0 is an arbitrary fixed x coordinate on the fault, and where

$$T(x) = p(x_0)\ (x - x_0) \cos \theta, \tag{3}$$

where $p(x)$ is the ray parameter and θ is the angle between the fault strike and the azimuth to the observer. Substituting (2) into (1), we obtain

$$U(t) \simeq \int_{z_1}^{z_l} \left[G(x_0, z, t) * \int_0^L \dot{D}(x, z, t) * \delta(t - T(x)) \frac{1}{\sin \delta}\, dx \right] dz. \tag{4}$$

For small changes in depth, z to z_0,

$$G(x_0, z, t) \simeq G(x_0, z_0, t). \tag{5}$$

Thus, we can rewrite (4) as

$$U(t) \simeq \sum_{k=1}^{l} G(x_0, z_k, t) * F_k(t), \tag{6}$$

where the z_k's are evenly spaced depths on the fault as shown in Figure 2, and where

$$F_k(t) \equiv \int_{z_k}^{z_{k+1}} \int_0^L \dot{D}(x, z, t) * \delta(t - T(x)) \frac{1}{\sin \delta} \, dx \, dz. \tag{7}$$

In other words, a finite fault can be approximated by a sum of point sources distributed over the depth range of the fault. The functions, $F_k(t)$, are the teleseismic time functions for each depth. In this study, we define the teleseismic time function of the entire earthquake as follows

$$F(t) \equiv \sum_{k=1}^{l} F_k(t - \tau_k), \tag{8}$$

where

$$\tau_k = z_k(1/\alpha^2 - p^2)^{1/2}, \tag{9}$$

and α is the P-wave velocity.

Notice that the ray parameter p and the observer azimuth θ are explicitly required in our definition of the time function, hence this time function changes from observer to observer. In other words, the above definition of the teleseismic time function is sensitive to source directivity effects. However, directivity plays an important role only when the rupture front progresses at a velocity which is roughly comparable with the seismic phase of interest. For waves viewed teleseismically, the horizontal phase velocity of wave fronts is much higher than the vertical phase velocity. Thus, directivity effects are much stronger in cases where rupture proceeds unilaterally up or down-dip, than in cases where rupture proceeds along the strike (Heaton, 1982). We conclude that the effects of source directivity on the teleseismic time function are significantly smaller than the effects of the overall rupture differences that are observed to occur between different earthquakes. However, knowledge of $U(t)$ for one observer does not allow us to uniquely invert equation (4) for $D(x, z, t)$ nor will it allow us to uniquely invert equation (6) to determine the time functions $F_k(t)$. Given motions from enough observers, we can deduce $D(x, z, t)$ as has been done by Kikuchi and Kanamori (1982) or by Hartzell and Heaton (1983). Kikuchi and Kanamori's (1982) definition of the total earthquake time function is very similar to ours, except that their formulation is a function of time only, which is equivalent to obtaining the time function for a station located infinitely far from the fault and whose P-wave ray path lies perpendicular to the fault plane. If the depth range of the fault is small when compared with the wavelengths of interest, then the fault can be approximated by a single point source.

In this case, the teleseismic time function can be computed from equation (6) by a simple deconvolution procedure such as that used by Boatwright (1980).

As we just discussed, the determination of the teleseismic time function $F(t)$ from knowledge of $U(t)$ at a single observer is an inherently underdetermined problem. In order to recast this as a well-posed inverse problem, we impose further assumptions about the nature of the individual depth time functions $F_k(t)$. Specifically, we assume that the functions $F_k(t)$ are nonnegative everywhere, that their integrated area is small, and that they may not vary as rapidly in time as $U(t)$. We now show how these assumptions allow us to rewrite equation (6) as a well-posed, linear, least-squares inverse problem. We begin by discretizing the problem as follows

$$u_i = U(i\ \Delta t); \quad i = 1, \cdots, n \tag{10}$$

$$g_i^k = G(x_0, z_k, \Delta t); \quad i = 1, \cdots, n; \quad k = 1, \cdots, l \tag{11}$$

and

$$\begin{aligned} f_j^k = F_k(j\ \Delta T) = F_k(jc\ \Delta t); \quad j = 1, \cdots, m; \quad k = 1, \cdots, l \\ c = \Delta T/\Delta t, \end{aligned} \tag{12}$$

where Δt is the sampling interval of the seismogram, and ΔT is the sampling interval of the time function. We sample the time function less often than the seismogram, hence c is a constant whose value is greater than 1. We can now rewrite equation (6) in component form as

$$u_i \simeq \sum_{k=1}^{l} \sum_{j=1}^{m} g_{i+(1-j)c}^k f_j^k. \tag{13}$$

We then define $\boldsymbol{A}$ to be the matrix with the following components,

$$A_{ij} = g_{i+c-jc+mc(k-1)}^k; \quad \text{for} \quad (k-1)m < j \leqq km. \tag{14}$$

We further define the vectors $\boldsymbol{X}$ and $\boldsymbol{b}$ to be given by

$$x_j = f_{j+(1-k)m}^k; \quad (k-1)\,m < j \leqq km, \tag{15}$$

and

$$b_i = u_i; \quad \text{for} \quad i = 1, \cdots, n. \tag{16}$$

Equation (13) can now be rewritten as

$$\boldsymbol{AX} \simeq \boldsymbol{b}, \tag{17}$$

where $\boldsymbol{A}$ is an n by lm matrix containing the earthquake impulse responses, $\boldsymbol{X}$ is an lm vector containing the time function, and $\boldsymbol{b}$ is an n vector containing the observation. As long as n is greater than lm, we have an inverse problem for $\boldsymbol{X}$ that is formally overdetermined. However, in many instances, $\boldsymbol{A}$ is a rather poorly conditioned matrix which, when inverted, may yield time functions having large

positive and negative spikes that destructively interfere to fit small, subtle phases in the records. To reduce these problems, we require that $\boldsymbol{X}$ be nonnegative everywhere, and we also minimize the overall size of $\boldsymbol{X}$ by including the following constraints as additional data to be satisfied

$$\lambda x_i = 0; \quad i = 1, \cdots, lm, \tag{18}$$

where λ is a nonnegative scalar weighting parameter. In this overdetermined least-squares problem, the inverse procedure trades off the overall fit of the synthetic to the data with the total moment of the earthquake. Increasing λ has the effect of decreasing the sum of the elements of the solution vector, which in this application is the moment. We can include the constraints in equation (18) by rewriting our inverse problem as

$$\left[\frac{\boldsymbol{A}}{\lambda \boldsymbol{I}}\right]\boldsymbol{X} \simeq \left[\frac{\boldsymbol{b}}{\boldsymbol{0}}\right]. \tag{19}$$

The study of equation (19) as a function of λ is called ridge regression or damped least-squares. We use the routine nonnegative least-squares from Lawson and Hanson (1974) to find the nonnegative $\boldsymbol{X}$ that gives the least-square error to the overdetermined problem given above. The advantageous properties of deconvolution by matrix inversion are also discussed by Bracewell (1965).

The methodology just discussed is very similar to that used by Ruff and Kanamori (1983), with the major difference being in the way the time function is made to be nonnegative. In our case, we find the unique nonnegative solution to the least-squares problem for a given value of λ. In other studies, the baseline of the time function is shifted after the inversion in order to produce a mostly positive solution (Kikuchi and Kanamori, 1982; Ruff and Kanamori, 1983; Beck and Ruff, 1984).

We now discuss the application of this methodology to the earthquakes considered in this study. A large, shallow subduction zone earthquake can have a fault plane with a length of hundreds of kilometers and a width of 100 km or more. For an average dip of 15°, the vertical extent of faulting is on the order of 25 km. As is shown in equation (6), we approximate a large finite fault with point sources that are evenly distributed over the depth range of the rupture. Throughout this study, we use four point sources that are each separated vertically by 7 km. Thus, the total depth range spanned is about 28 km.

Figure 3 illustrates a typical fault model. The velocity structure in Figure 3 is based on work by Taber (1983) for the continental margin of Washington. This structure is used as the source structure for every earthquake studied, regardless of its location. Changing the velocity structure from region to region is not warranted. First, little is known about the velocity structures of many continental margins, and second, a uniform half-space model would yield very similar results. The teleseismic Green's functions in Figure 3 are for four typical depths and include the responses of all rays with up to two internal reflections in the layered stack. All conversions between phases occurring at the free surface are included as well as the more important internal conversions. Despite the addition of all these rays, the Green's functions are dominated by the phases P, pP, and sP. Therefore, we feel justified in not varying the velocity structure from location to location.

For each earthquake in Figure 1, four teleseismic Green's functions are computed using the four depths and the fault plane information given in Table 1. All fault parameters in Table 1 are taken from the literature. The four depths bracket the hypocentral depth. In some cases, indicated by a * in Table 1, a published fault plane solution could not be found. For these events, the mechanism is estimated from the strike and dip of the trench. In a few instances, the published mechanism is inconsistent with the first motion at Pasadena. In these cases, the dip or strike (value in parentheses in Table 1) is adjusted by a small amount to obtain the correct first motion. The Green's functions are convolved with a boxcar time function with a 0.9-sec duration. The width of this time function sets the minimum time resolution of the inversion and corresponds to ΔT in equation (12). Attenuation is entered

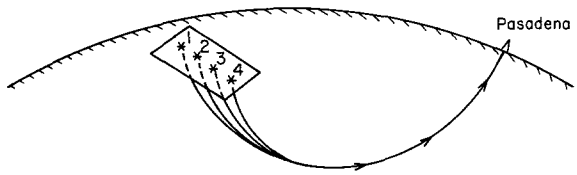

Velocity Structure

α(km/sec)	β(km/sec)	ρ(gm/cm³)	h(km)
5.00	2.88	2.40	8.0
5.80	3.34	2.50	9.0
7.00	4.04	2.75	13.0
8.00	4.62	2.90	—

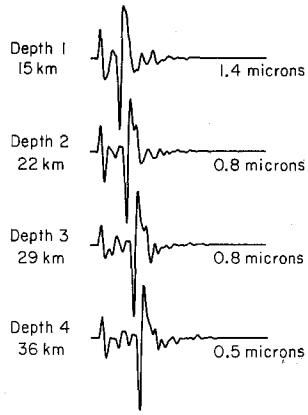

FIG. 3. Schematic illustration of the discretized fault model and table of the velocity structure used. Typical Green's functions (50 sec long) are shown for a 1–90 instrument and four source depths.

with the Futterman Q operator (Futterman, 1962) with constant $t^* = T/Q = 1.0$ (Carpenter, 1966), where T is the ray travel time, and Q is the average seismic quality factor along the ray. The Green's functions are passed through a Benioff 1–90 instrument response and processed in an identical manner as the data, with a 1- to 60-sec Butterworth bandbass filter and a 0.2-sec sample spacing. Here, 0.2 sec corresponds to Δt in equations (10) and (11).

The teleseismic source time functions, $F_k(t)$, for each of the four source depths are obtained simultaneously by solving the least-squares problem illustrated in Figure 4 and given by equation (19). The columns of the $\boldsymbol{A}$ matrix contain the processed Green's functions for the four different source depths. For a given depth, the Green's function in any column of $\boldsymbol{A}$ is phase shifted by the amount $\Delta T = 0.9$ sec from the Green's function in the column to its left. $\boldsymbol{b}$ is the data vector containing the digitized vertical 1–90 record, and $\boldsymbol{X}$ is the solution vector of the teleseismic

source time functions for the four different source depths. The value of the damping parameter λ is selected by a trial-and-error process by trading off the fit to the data for the moment of the solution. Once selected the same value of λ is used for all records. The effect of the damping parameter will be discussed further in the following section when the deconvolution results are presented.

Figure 5 shows two examples of deconvolutions of 1–90 records; event 1, a 1971 8.0 M_W Solomon Islands earthquake, and event 22, the 1968 8.2 M_W Tokachi-Oki earthquake. The teleseismic time functions for the four different source depths are shown as well as the stacked sum. The vertical scales are in units of 10^{26} dyne-cm. The time functions have been shifted by the difference in travel times for the

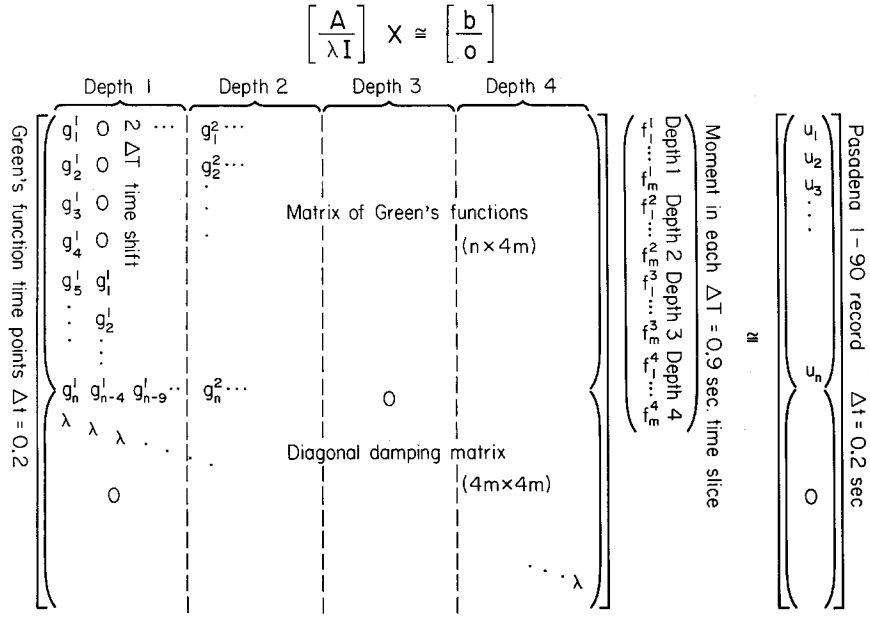

FIG. 4. The damped least-squares problem that is solved to deconvolve propagation and instrument effects from the Pasadena Benioff 1–90 records.

different source depths. Therefore, the summed time function is an estimate of the total moment release, from the top to the bottom of the fault, as a function of time and as viewed from Pasadena. Below the time functions, the vertical 1–90 records are compared with the synthetic records obtained by convolving the Green's functions for the four source depths with the appropriate time functions. The comparison with the data is good and typical of the fit obtained for the 63 earthquakes studied.

SOURCE TIME FUNCTIONS

Figures A1 through A19 in the Appendix show the teleseismic source time functions for the 63 earthquakes listed in Table 1 and plotted in Figure 1. The earthquakes are grouped according to the subduction zone where they occurred, and within a given region, from the largest (at the top) to the smallest (at the bottom). The seismograms are plotted on the left-hand side of each figure. The records are all Pasadena or Barrett, vertical 1–90 recordings with the exception of the 1964 Alaska earthquake (event 47), for which the Pasadena, rotated radial Wood-

Anderson record is used. Small arrows below each trace indicate the section of the seismogram used to compute the time function. This time interval varies from event to event and is adjusted to include most of the *P*-wave energy, but not any obvious

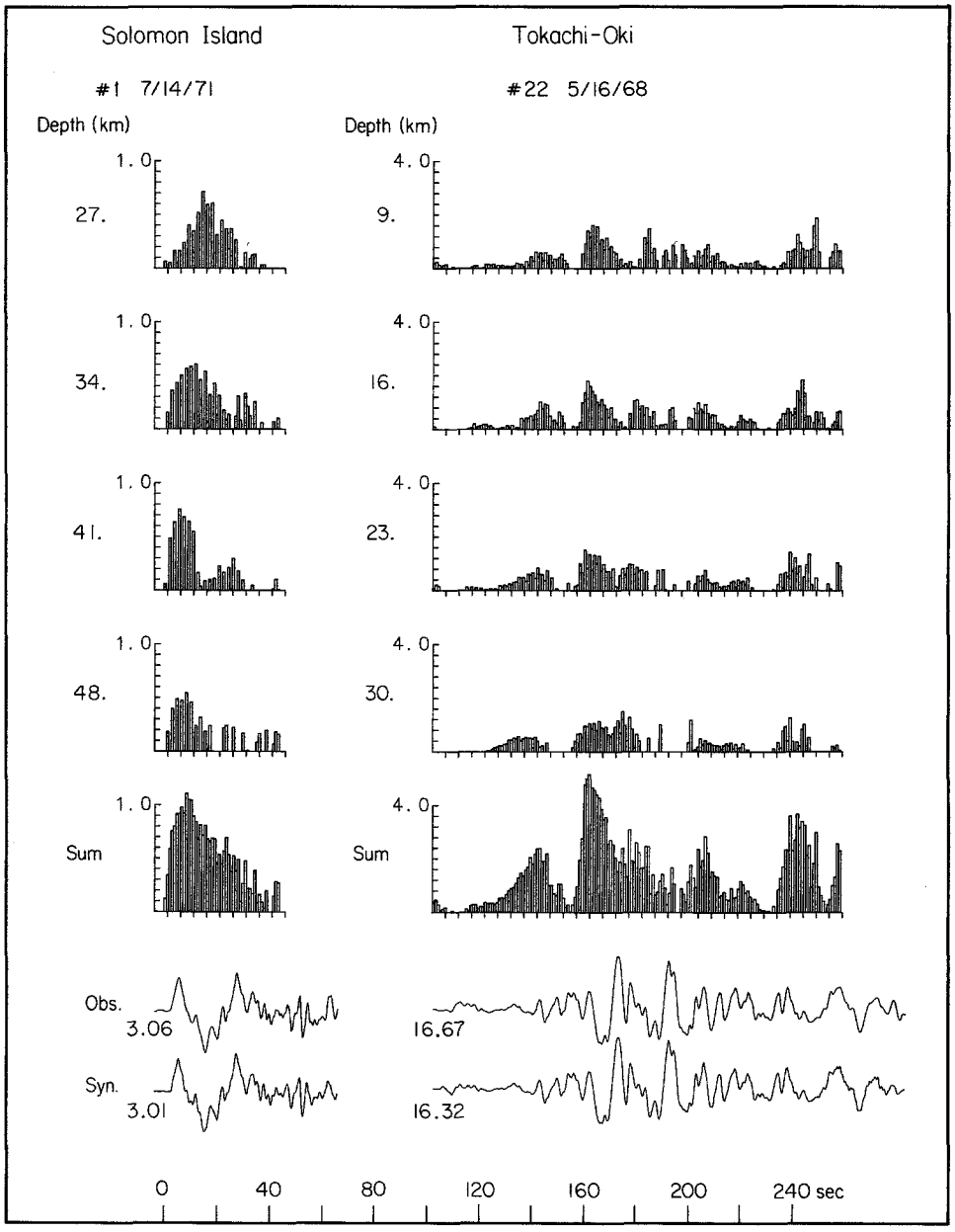

FIG. 5. Two examples of stacking of the time functions for four source depths and the comparison of the convolution of the time functions with the appropriate Green's functions (synthetic) and the original data record (observed). Vertical scales for the time functions are in units of 10^{26} dyne-cm.

PP phase. (The longer time interval for event 1 in Figure A1 was used to compare with the unpublished work of M. Kikuchi.) The numbers above each trace refer to the event numbers in Table 1 and Figure 1. The peak record amplitude, corrected

for the gain of the instrument, is given in microns below each record. To the right of each seismogram, the time function is plotted twice; first, using a variable self-scaling plot so that the details of the time function are visible, and second, using a constant full-scale amplitude plot allowing easy comparison of the size of events. Only the sum of the time functions for the four individual deconvolution source depths is plotted. The vertical scales for the time function plots are in units of 10^{26} dyne-cm. The same horizontal time scale is used for all the time functions as well as the plots of the P waveforms.

In Figure A2 and A14, the formats are slightly different. The Pasadena 1–90 record could not be found for the 1944 Tonankai earthquake. This earthquake occurred in the Nankai Trough of southwestern Japan and has a location, focal mechanism, depth, and moment very similar to the 1946 Nankaido earthquake (Kanamori, 1972a). The Nankai Trough is a young subduction zone (age ~ 20 m.y.) and has been the site of several magnitude 8 earthquakes. Because the Tonankai earthquake is a significant event, Figure A2 shows a comparison of Nankaido and Tonankai P waveforms recorded on the same instrument, a vertical Galitzin seismometer at Copenhagen, Denmark. Since these two earthquakes have such similar fault parameters, this one-station comparison has some validity. From an examination of the P waves at Copenhagen, the Nankaido earthquake appears to be a more complex event than does the Tonankai earthquake. Figure A14 also requires some additional explanation. The foreshock in Figure A14 occurred approximately 15 min before the 22 May 1960 M_w 9.5 Chile earthquake. Contamination of the main shock record by the foreshock is not significant for the purposes of this study. The amplitude of the foreshock wave train is about 10 per cent of the main shock body-wave amplitudes.

The period bandwidth over which the time functions are considered reliable is from 50 to 2.5 sec. The long-period limit is due primarily to the rolloff of the instrument response at longer periods. The short-period limit is a consequence of both digitizing noise and the frequency limit of the discretized time function used in the deconvolution. As discussed in the previous section, the time function is formed by calculating the proper weights for a series of phase-shifted sources with narrow boxcar time functions with widths of 0.9 sec. Adjacent sources have a tendency to interfere with one another, brought about by the fact that an idealized, discretized source is being used to model a continuous, finite source. The period of this interference is 1.8 sec. Figure 6 compares two spectra which illustrate this process. Both spectra are for events 105 (North Honshu) in Figure A4. The solid curve is the spectrum of the source time function obtained by the least-squares inversion technique with positivity constraint, but using one source depth of 33 km instead of four. The dashed curve is the spectrum of the 1–90 record divided by the spectrum of a single Green's function of the same source depth of 33 km. In the least-squares inversion spectrum, a small interference peak can be seen, centered at 1.8 sec. However, within the bandwidth of 50 to 2.5 sec, the spectra agree quite well, except for some differences in spectral peaks. In terms of the time functions in Figures A1 to A19, high reliability should not be placed on the amplitude of individual 0.9 sec slices (width of individual boxcars in plots). The higher spectral level at periods longer than about 60 sec for the least-squares inversion in Figure 6 is due to the positivity constraint.

The accuracy of the calculated source time function depends on using the correct Green's function in the deconvolution. As noted above, the form of the Green's

function is not particularly sensitive to the layered velocity structure used. However, the Green's function is sensitive to the focal mechanism, particularly near a node in the radiation pattern. In Figures A3 and A18, event 19 (Central Honshu) and events 88, 89, and 90 (Izu Bonin-Marianas) are nodal at Pasadena and yield atypical time functions compared with other nonnodal earthquake records with similar magnitudes. For this reason, these deconvolutions are considered to be less reliable. Also, the Green's functions used do not include the phase *PP*. *PP* arrives about 1 min after *P* at a distance of 30° and about 3.5 min after *P* at a distance of 90°. In most of the 1–90 records we studied, *PP* is not an obvious arrival and is hidden by the *P*-wave coda. Inversion of the *P*-wave coda and the phase *PP* using our simple Green's function will contribute errors to the latter part of the time function.

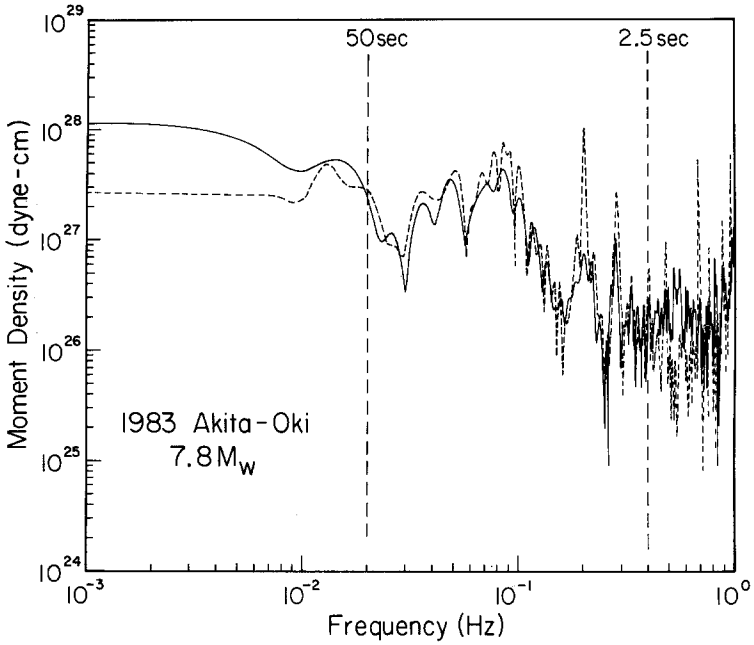

FIG. 6. Comparison of Fourier amplitude spectrum of the Akita-Oki 1–90 record divided in the frequency domain by the Green's function for a single source depth of 33 km (dashed curve), and the spectrum of the time function obtained by damped least-squares deconvolution using the same Green's function (solid curve).

Besides the Green's function, the choice of the least-squares damping parameter is also an important control on the form of the source time function. As mentioned previously, the same damping parameter is used for all events. This action was taken in the interest of developing a standard processing procedure to facilitate the study of a larger number of earthquakes. However, for records with higher noise levels or with poorly determined or variable focal mechanisms, more damping may be appropriate. This situation is characterized in Figures A1 to A19 by a time function which maintains significant amplitude later in the *P*-wave record, where there is little arriving energy. Examples where this difficulty occurs are event 80 (Central America) in Figure A10 and the previously mentioned nodal events.

A damping scheme which might be more effective in reducing the above difficulties is one in which the damping parameter, λ, increases linearly from the beginning of the record to the end (L. Ruff, personal communication). In many cases the 1–90 *P*

wavetrain is a long and complicated record. The later parts of the seismogram undoubtedly contain more scattered energy, which is not relevant to our study of the source. A linearly increasing functional form for λ would more heavily damp the sections of the seismogram containing more scattered energy and reduce their contribution to the computed source time function. Alternatively, if seismograms are available from several stations at a wide range in azimuths, it should be possible to estimate at what time scattered energy becomes the dominant arrival. Since the character of scattered energy is highly path-dependent, and the direct-source P-wave energy is much less path-dependent, the source time functions at different stations should look similar until the time scattered energy dominates the record. Therefore, by comparing deconvolutions at different stations, one could derive an optimum distribution for λ which would maximize the moment contribution from the coherent sections of the seismograms. However, multiple 1–90 records at different azimuths are not available for most of the earthquakes we studied. The procedure we use of applying a constant damping parameter to all seismograms is the simplest one, other than no damping. In some cases, this practice may lead to too much moment contribution from the latter parts of the P-wave seismogram. If data is available from other sources, indicating a shorter length to the actual source time function, the later part of the time function in this study can be disregarded. This process does not lessen the validity of the initial part of the time function.

Obvious water-layer multiple reflections are not prevalent in the P waveforms, although these multiples can be quite strong for smaller earthquakes with steeply dipping fault planes (Ward, 1979). Some of the smaller events from the Kuriles (Figure A6) may contain water multiples. Event 27 has a periodic waveform which is characteristic of a multiple. Event 30, also from the Kuriles, has a strong 20-sec periodicity in the time function which may be due to a water-layer multiple. But, in general, the characteristic ringing of the P wave, indicative of a water multiple, is not observed.

Events 92 and 98 (Chile) in Figure A16 may not be shallow thrust earthquakes related to the down-going plate. These two events are located significantly inland from the trench (see Figure 1), although there may be considerable error in their location. Little is known about these two earthquakes, and their focal mechanisms have been estimated from the trench orientation. For these reasons, they should be considered separately from the other Chile earthquakes. Another event which requires some qualifying remarks is event 41 (Aleutians) in Figure A8. This event may not be an earthquake, but rather a large underwater landslide (Hiroo Kanamori, unpublished data). Although this event has a surface wave magnitude of only 7.4, it produced a very large tsunami with a tsunami magnitude of 9.3. The long-period nature of the source can be seen by examining the P waveform in Figure A8. The beginning of the record is dominated by a long-period, one-sided pulse, which when deconvolved, yields a source pulse with a duration of 1 min or more. These characteristics could be explained by a landslide.

The area under the source time functions in Figures A1 to A19 should equal the moment of the earthquake. However, given the limited bandwidth of the data, the body-wave estimate of the moment will saturate for sufficiently large earthquakes. There is also a question of how the positivity constraint and the damping parameter in the deconvolution affect the moment estimates. Figure 7 compares the moment estimated from the area under the time function with the published moment for the earthquake. The published moments are usually based on long-period surface

wave amplitudes (references in Table 1), but no attempt has been made to check their accuracy. The dashed curve in Figure 7 indicates equality of the two estimates. The points follow the trend of the equality curve up to a moment of about 2.5×10^{28} dyne-cm (moment magnitude of 8.2), at which point saturation occurs. Below the saturation level, the estimates of moment from the time functions, on average, run less than the long-period surface wave moments. This observation has been noted in other studies and is probably due to longer period fault slip not well resolved by band-limited body-wave records. A few of the time function moment estimates are unusually low. Many of these are from nodal records or older earthquakes for which the published moment may be less well determined (such as events 17, 18, and 19 in Japan). The low estimate for event 47, the 1964 Alaska earthquake, is due to the use of a Wood-Anderson record, which has a considerably lower long-period response. However, in general, the estimates of moment from the least-squares inversion are consistent with other body-wave estimates and do not exhibit any anomalous behavior. For the largest earthquakes, above the saturation

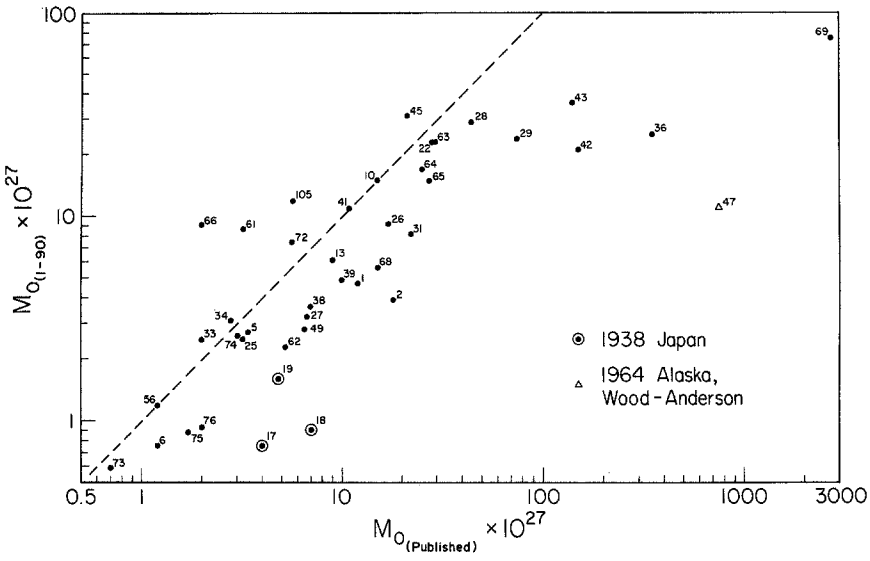

FIG. 7. Comparison of moment estimated from the area under the time function curve with the published long-period moment.

level, the time functions in Figures A1 to A19 are misleading because of the large amount of missing moment. In Figure 8, the time functions for the six largest earthquakes are replotted so that the area under the curve is equal to the long-period surface wave moment. The missing moment has been added using a sine wave functional form with a period equal to twice the record length used in the inversion. This representation gives a very smooth time function. However, the solution is not unique. The missing moment could be added in any way such that it lies outside the pass band of a 1–90 instrument. The time functions in Figure 8, besides giving a good representation of the relative sizes of the events, probably represent the smoothest end members of allowable models.

It is difficult to find meaningful comparisons of the time functions in Figures A1 to A19 with the work of other authors. This difficulty exists for the following reasons. If stations are considered individually, as in this study, the computed time function can vary from station to station due to directivity effects and local site

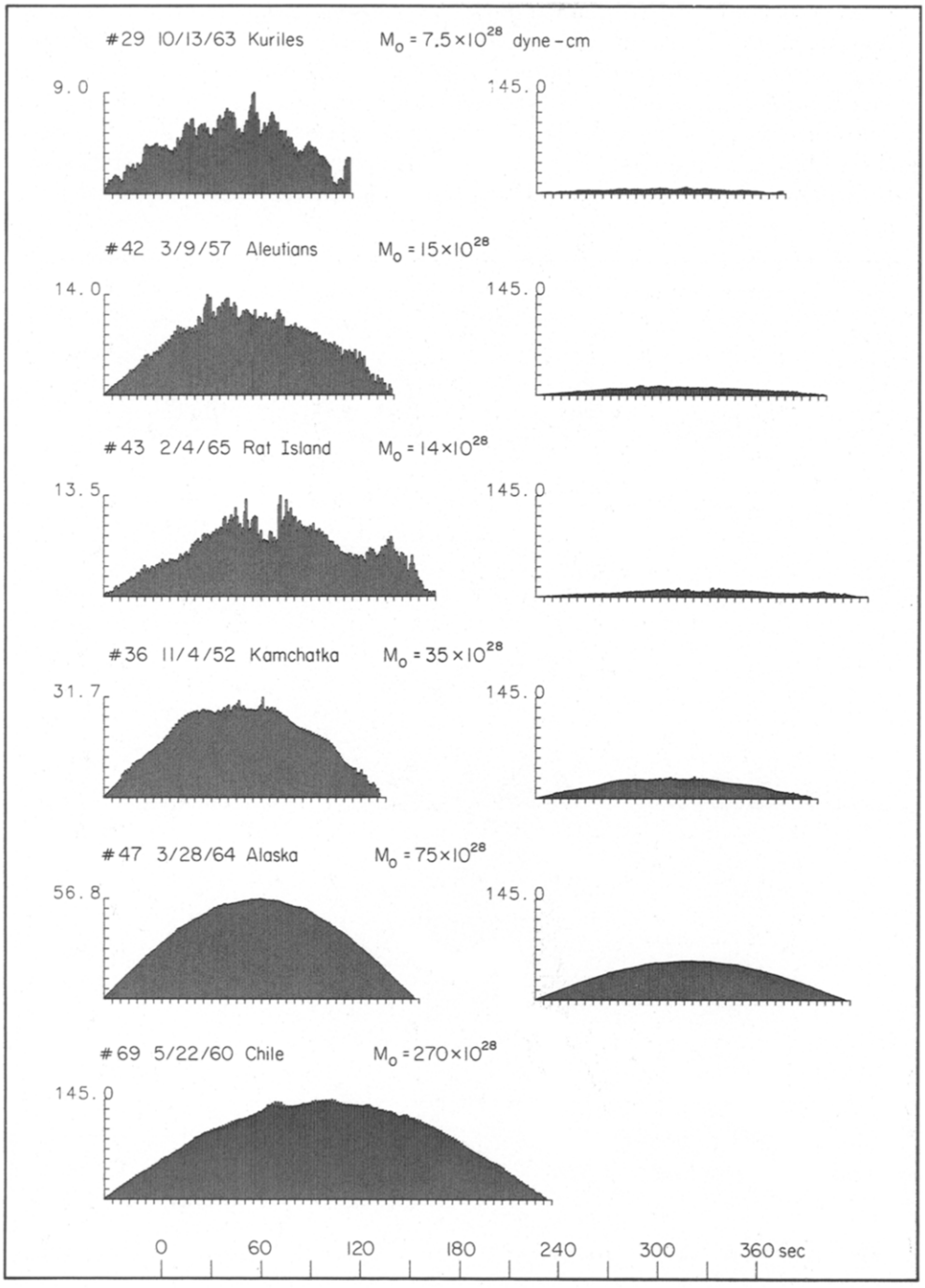

FIG. 8. Time functions for the six largest earthquakes considered in this study. The difference between the body-wave estimate of the moment and the long-period moment has been added to the time functions of Figures A1 to A19. Vertical scales for the time functions are in units of 10^{26} dyne-cm.

effects. Ruff and Kanamori (1983) and Beck and Ruff (1984) give some examples of the azimuthal variability. Other important considerations in comparing results are the deconvolution technique used and the frequency bandwidth of the data. With these points in mind, Figure 9 compares eight time functions from this paper

with the results of several other studies. The time function for the 1971 Chile earthquake, from Malgrange *et al.* (1981), is based on forward modeling of long-period *P* waves from WWSSN stations. It is interesting to note that the shoulder on their basically trapezoidal time function is well resolved in the deconvolution of the 1–90 record. The time function for the 1958 Ecuador earthquake, after Beck and Ruff (1984), is an average of several deconvolutions of long-period stations in North America. The time functions labeled with a circled 3 in Figure 9 are from

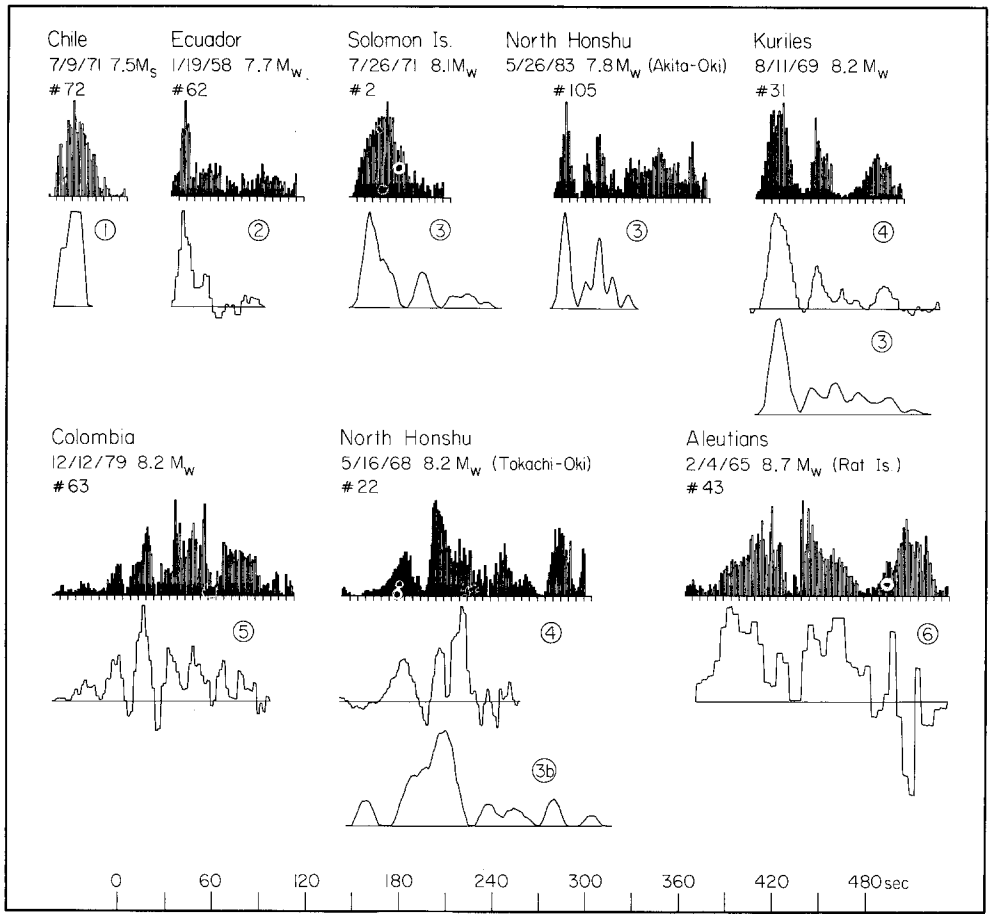

FIG. 9. Comparison of eight time functions from this study with the results of other authors: (1) Malgrange *et al.* (1981); (2) Beck and Ruff (1984); (3) M. Kikuchi, unpublished work; (3b) Kikuchi and Fukao (1984); (4) Schwartz and Ruff (1985); (5) S. Beck and L. Ruff, unpublished work; and (6) Ruff and Kanamori (1983). See text for details.

Kikuchi and Fukao (1984) and other unpublished work by M. Kikuchi using a technique discussed by Kikuchi and Kanamori (1982). These time functions are obtained by a simultaneous inversion of several *P* waveforms from WWSSN stations. The time functions have had the azimuthal dependence of the source removed and are an estimate of the moment release as a function of time only. If the earthquake source were a point source, then the time function from the single Pasadena 1–90 record should be the same as the Kikuchi time function. Even though this condition is not met, there are some strong similarities between the time functions, particularly for the 1968 Tokachi-Oki and 1983 Akita-Oki earthquakes.

Schwartz and Ruff (1985) also studied the Tokachi-Oki earthquake and the 1969 Kuriles earthquake using WWSSN records. Their estimates of the time functions for these two events, based on single station deconvolutions, are shown in Figure 9. Stations were selected from the ones they considered which have takeoff azimuths most similar to that of Pasadena (i.e., TUC for Tokachi-Oki and WES for Kuriles). The time function for the 1979 Colombia earthquake is from unpublished work by S. Beck and L. Ruff. They deconvolved the same 1–90 record used in this study, but by the method of Ruff and Kanamori (1983). The only difference between the two deconvolutions is in the treatment of the long-period baseline. The two estimations of the time function are very similar. The time function for the 1965 Rat Island earthquake is from Ruff and Kanamori (1983) and is based on the BUL WWSSN record. Making allowances for the differences in data and the differences in analysis, the time functions in Figure 9 compare favorably.

Spectra

Fourier amplitude spectra have been computed for each of the 1–90 P waveforms in Figures A1 to A19. The spectra of the eight largest events are shown in Figure 10, a and b. Spectral amplitudes are plotted over the period range of 1 to 60 sec. The spectra are most reliable from 2 to 50 sec. Corrections are made for propagation effects and the response of the instrument in the following manner. A synthetic is calculated for the direct P wave only, using the focal mechanism in Table 1. Attenuation is added assuming a $t^* = 1.0$. The synthetic is processed in the same way as the data records, including the bandpass Butterworth filter and the 1–90 instrument response. The spectrum of the data record is then divided by the spectrum of the P-wave synthetic to give the source spectra in Figure 10. Figure 10 also shows the spectrum of the P-wave impulse response plotted using the expanded vertical scale to the right and superimposed over the 1960 Chile and 1963 Kuriles spectra. If a complete ray set were used, instead of just the direct P wave, the synthetic spectrum in Figure 10 would be scalloped, primarily due to the interference of P, pP, and sP. However, the overall shape of the spectrum of the impulse response would be very similar, and thus the shape of the inferred source spectrum would not be changed significantly.

Given the limited bandwidth of the data, only a portion of the spectrum is resolvable (2 to 50 sec). Therefore, for the larger events, the spectral parameters of corner frequency and zero-frequency asymptotic level cannot be measured. However, the slope of the spectrum between 2 and 50 sec can be accurately measured. Table 2 lists the power of the falloff of the source spectra for the events in Table 1. The slopes vary from $\omega^{-1.00}$ to $\omega^{-2.25}$, with an average of $\omega^{-1.5}$. These values depend on the assumed attenuation level ($t^* = 1.0$). To obtain an average spectral falloff of ω^{-2} from these data would require an average t^* of about 0.5. To further investigate the shape of the source spectra, smoothed spectra were computed for all earthquakes and sorted into five different magnitude intervals: 7.0 to 7.5; 7.5 to 8.0; 8.0 to 8.5; 8.5 to 9.0; and 9.0 to 9.5. These spectra are shown in Figure 11, a to c. The procedure used to compute these spectra is similar to that used to compute the spectra in Figure 10. However, scaling for the radiation pattern is treated somewhat differently and is discussed below. The spectra in Figure 11a (upper left-hand corner) are obtained by averaging the logarithmic values of all the spectra within the five different magnitude intervals. Although the individual earthquakes show a large variation in spectral shapes, the average spectrum for each magnitude interval has a spectral falloff of $\omega^{-1.5}$.

Since the vertical scales in Figures 10 and 11 are in terms of moment, it is important to clearly state the scaling which is used to go from far-field displacements to moment. At teleseismic distances, the zero-frequency spectral level for an incident

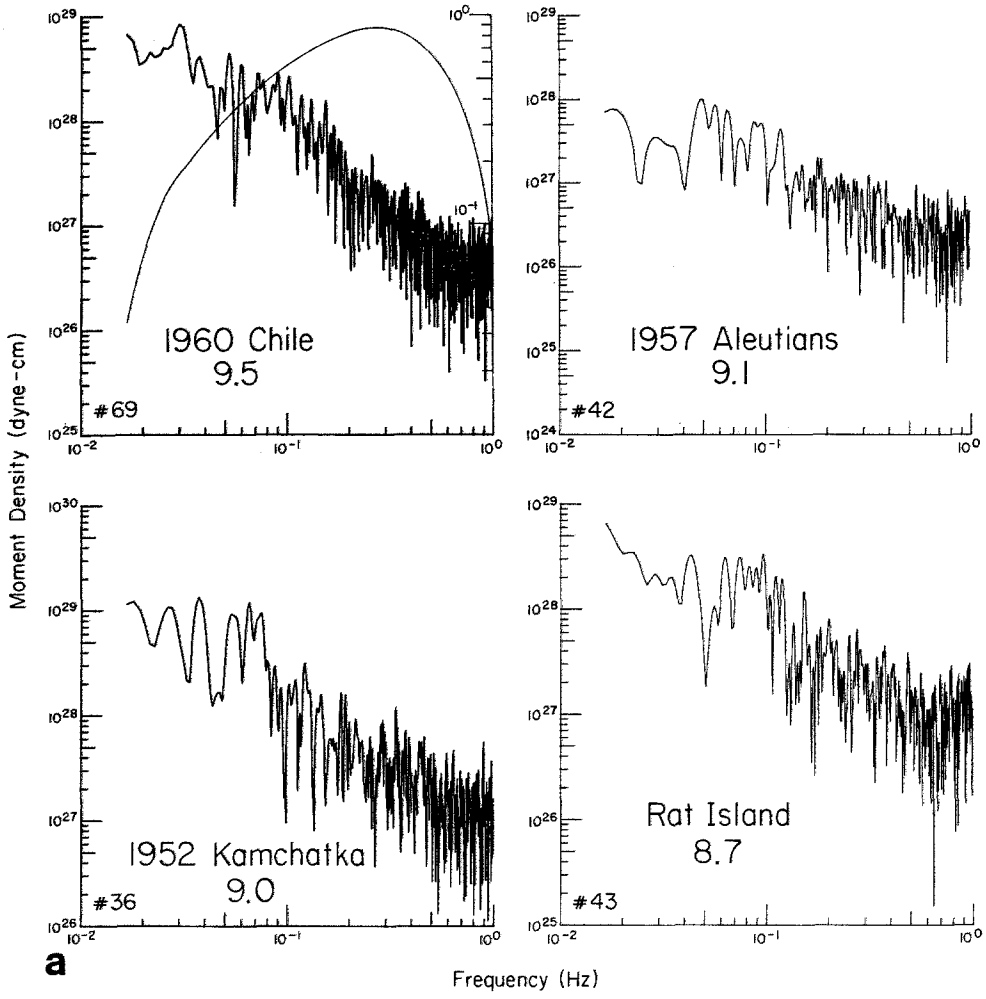

FIG. 10. (a) Fourier amplitude spectra of selected Pasadena 1–90 P-wave records. See text for details. (b) Same as (a).

P wave, $|\tilde{U}(0)|$, is related to the moment, M_0, by (Helmberger, 1983)

$$|\tilde{U}(0)| = \frac{M_0}{4\pi\rho} \sum_{j=1}^{3} \left[C_j(p)\, A_j \right] R_{PZ}(p)\, \frac{g(\Delta, h)}{a}, \tag{20}$$

where π is the density in the source region, $C_j(p)$ are the vertical radiation pattern terms, A_j are the horizontal radiation pattern terms, $R_{PZ}(p)$ is the receiver function, $g(\Delta, h)$ is the geometrical spreading factor, p is the ray parameter, and a is the radius of the earth. For the spectra in Figure 10, the values of $C_j(p)$, A_j, and $R_{PZ}(p)$ are set consistent with direct P-wave radiation from a source with the mechanism given in Table 1. For cases where P is not the dominant phase in the record, this

procedure will bias the spectral amplitudes, but not the spectral shapes. That is, for cases where P is near-nodal, the phases pP or sP may still be relatively strong, and thus spectral amplitudes may be overestimated. For this reason, the spectra in

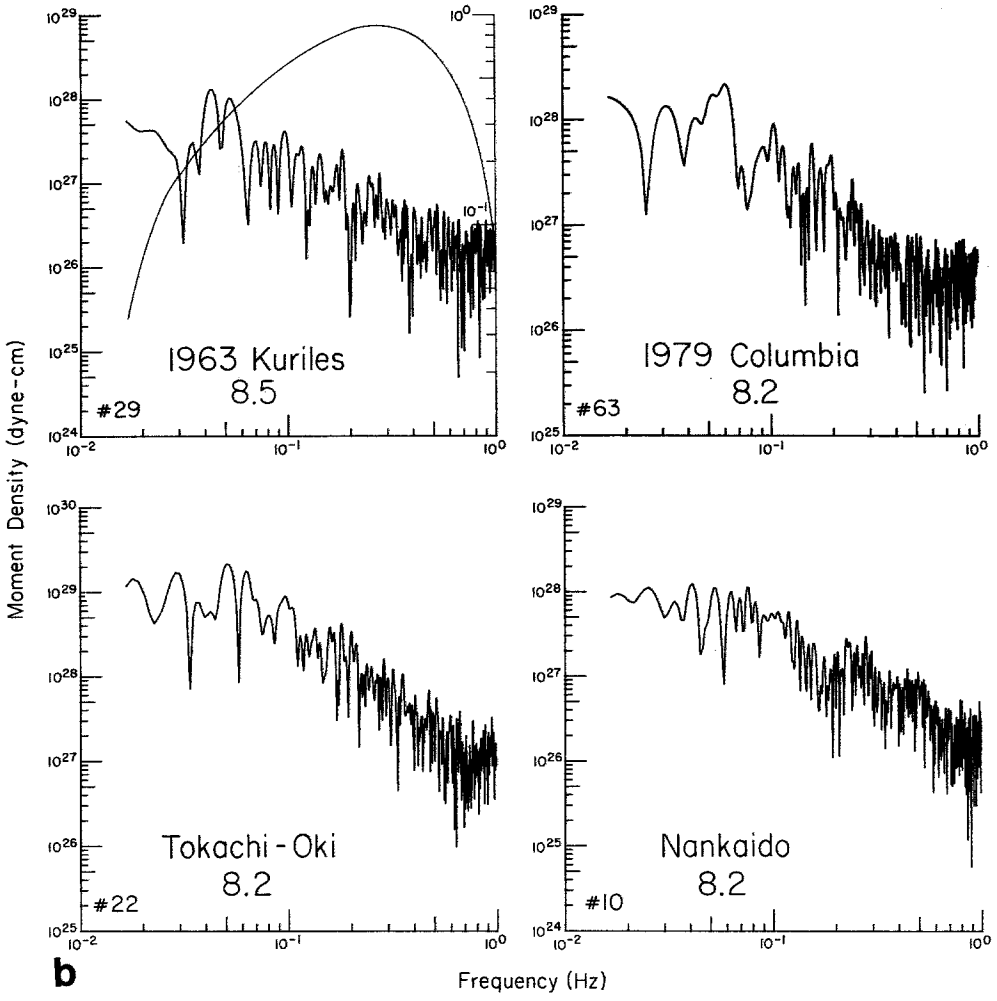

FIG. 10b

Figure 11 are computed using the same average P-wave radiation pattern coefficient for each event. The following values for the variables in equation (20) are used: $A_1 = A_3 = 0$; $A_2 = 0.707$; $C_2 = 1.56 \times 10^{-2}$; $R_{PZ} = 0.171$; $p = 0.088$ sec/km; and P-wave velocity, S-wave velocity, and density in the source region of 8.0 km/sec, 4.62 km/sec, and 2.9 gm/cm^3, respectively. We should note that equation (20) is often expressed as (Chung and Kanamori, 1976)

$$|\tilde{U}(0)| = \frac{M_0}{4\pi\rho} \frac{C(i_0)}{\alpha^3} R_{\theta\phi} \frac{g(\Delta, h)}{a}. \tag{21}$$

where $C(i_0)$ is the receiver coefficient given by Bullen's (1963) equation [8(16)], $R_{\theta\phi}$

TABLE 2

SPECTRAL SLOPES BETWEEN 2 AND 50 SEC

Event No.	Magnitude (M_w)	Slope	
1	8.0	−1.20	
2	8.1	−1.33	
5	7.7	−1.30	
6	7.4	−2.13	
10	8.2	−1.20	1946 Nankaido
13	7.9	−1.40	
18	7.7*	−1.26	
19	7.8*	−1.60	
22	8.2	−1.70	1968 Tokachi-Oki
23	7.5*	−1.60	1968 Hyuganada
24	7.2*	−1.20	
25	7.7*	−1.50	1978 Sendai
26	8.1	−1.80	1952 Hokkaido
27	7.8	−1.80	
28	8.3	−1.60	1958 Kuriles
29	8.5	−1.33	1963 Kuriles
30	7.3*	−1.90	
31	8.2	−1.60	1969 Kuriles
33	7.4	−1.33	
34	7.6	−1.25	
36	9.0	−1.70	1952 Kamchatka
37	8.2	−1.23	1959 Kamchatka
38	7.8	−2.00	
39	7.9	−1.30	
41	7.4*	−1.23	
42	9.1	−1.43	1957 Aleutians
43	8.7	−1.40	1965 Rat Island
45	8.2	−1.30	1938 Alaska
49	7.7*	−1.30	
56	7.4	−1.40	
61	7.9*	−1.20	
62	7.7	−1.20	
63	8.2	−1.70	1979 Columbia
64	8.2	−1.30	1940 Peru
65	8.2	−1.20	1942 Peru
66	8.1	−1.35	1966 Peru
68	8.1	−1.60	1974 Peru
69.B	7.8†	−1.70	1960 Chile foreshock
69	9.5	−2.00	1960 Chile
72	7.5*	−1.40	
73	7.0*	−1.35	
74	7.5*	−1.80	
75	7.0*	−1.50	
76	7.2*	−2.05	
80	7.9*	−2.05	
81	7.1*	−1.50	
84	7.5*	−1.75	
85	7.7*	−1.40	
86	7.3*	−2.00	
88	7.2*	−1.40	
90	7.1*	−1.00	
91	8.3*	−1.70	
92	7.4*	−1.15	
97	7.7*	−2.25	
98	7.4*	−1.20	

TABLE 2—*Continued*

Event No.	Magnitude (M_w)	Slope	
99	7.4*	−1.30	
100	7.8*	−1.60	
102	8.0*	−1.50	
103	7.6*	−1.50	
105	7.8	−1.90	1983 Akita-Oki
		Average −1.5	

* M_S.
† Duda.

is the P-wave radiation pattern term (both horizontal and vertical), and α is the P-wave velocity in the source region. A typical average value for $C(i_0)$ for P waves at teleseismic distances is 1.5. An average value for $R_{\theta\phi}$ for low-angle thrust faults at teleseismic distances is 0.78 (Boore and Boatwright, 1984). When these values are used in equation (21), they yield a spectral level within 20 per cent of the values we have used in equation (20).

The source spectral amplitude for a uniform rupture with a ramp near-field time function over a rectangular fault plane in a whole-space is given by (Mikumo, 1971)

$$|\tilde{U}(\omega)| = \frac{M_0 R_{\theta\phi}}{4\pi\rho R\beta^3} \left|\frac{\sin(\omega X_\tau)}{\omega X_\tau}\right| \left|\frac{\sin(\omega X_L)}{\omega X_L}\right| \left|\frac{\sin(\omega X_w)}{\omega X_w}\right| \tag{22}$$

where X_τ, X_L, and X_w are duration times associated with the rise time, fault length, and fault width. The above spectrum has a high-frequency falloff of ω^{-3}. Depending on the relative values of X_τ, X_L, and X_w, sections of the source spectrum can have slopes of ω^{-1}, ω^{-2}, or ω^{-3}. Although we do not advocate this particular simplictic model, it is not difficult to postulate source models which produce quite different spectral falloffs, such as those in Table 2.

Another way of affecting the slope of the source spectrum is by introducing heterogeneities on the fault plane. A statistical distribution of fault strength or stress drop with variable length scales will decrease the high-frequency spectral falloff (Haskell, 1966). If the irregularities are given a uniform spatial or temporal distribution, an inflection in the spectrum can result. Aki (1983), presenting work by Gusev (1983), discusses a source spectrum for large earthquakes (M~8) where the spectral slope changes from ω^{-2} to ω^{-1} to ω^{-3} in going from periods of 60 to 10 to 0.1 sec. This source model results in an inflection in the spectrum centered around 10 sec and is postulated as being due to a regular barrier or roughness interval on the fault. The spectra of the 1–90 records cannot resolve which of the above source models is the most appropriate. However, they may argue for a different source model than the frequently cited simple ω^{-2} source model for all larger earthquakes.

Discussion of Results

The teleseismic source time functions presented in this paper have two main applications: (1) to obtain a better understanding of the generation and worldwide distribution of major shallow thrust subduction zone earthquakes; and (2) to obtain estimates of the frequency content of the seismic radiation from these sources for engineering design purposes. First, consider the engineering applications. Few strong

motion records exist for subduction zone earthquakes. Besides isolated records from Mexico and South America, the only sizable strong motion data set is from Japan (Mori and Crouse, 1981), and most of these records are for distances greater than 50 km. One way to obtain bench marks on the type of strong ground motion likely to occur in other subduction zones or at closer-in distances is to use teleseismic data. The Benioff 1–90 instrument is particularly suited to this application because of its broad bandwidth and good response at 1 sec. For a subduction zone with no recorded strong ground motion, the earthquake source parameters can be partially

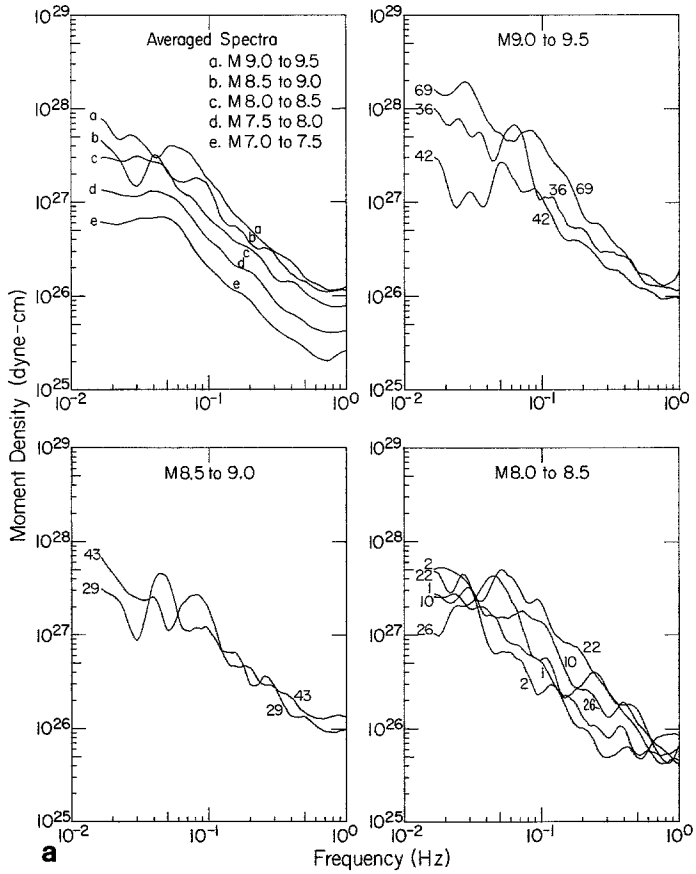

FIG. 11. (a) Smoothed *P*-wave Fourier amplitude spectra for the events listed in Table 1 and grouped according to five magnitude intervals. (b) and (c) same as (a).

constrained by requiring them to satisfy teleseismic body-wave recordings of previous events. This source description can then be used to compute near-source strong motion records. A variation of this approach involves comparison of similar subduction zones. The Japan trench has produced a fairly large set of strong motion records. If it is determined that another trench produces similar size earthquakes with similar teleseismic source time functions as earthquakes from Japan, then it may be justified to use the Japanese strong motion data set for design purposes in the second region.

Recent studies of large subduction zone earthquakes suggest that the maximum observed earthquake for a given trench is directly related to the degree of coupling between the plates and the size of fault asperities (Uyeda and Kanamori, 1979; Lay

et al., 1982; Ruff and Kanamori, 1980, 1983). Ruff and Kanamori (1980) found a significant relationship between the age of the subducting lithosphere, convergence rate, and the maximum M_w. Trenches subducting younger crust with higher convergence rates were found in general to produce larger earthquakes. Higher convergence rates and younger, more buoyant crust are thought to cause larger earthquakes by producing strong coupling between the plates. In the asperity model of subduction zone earthquakes, stronger coupling is a direct result of greater areas of the fault plane supporting the accumulated stress between the plates. These areas rupture

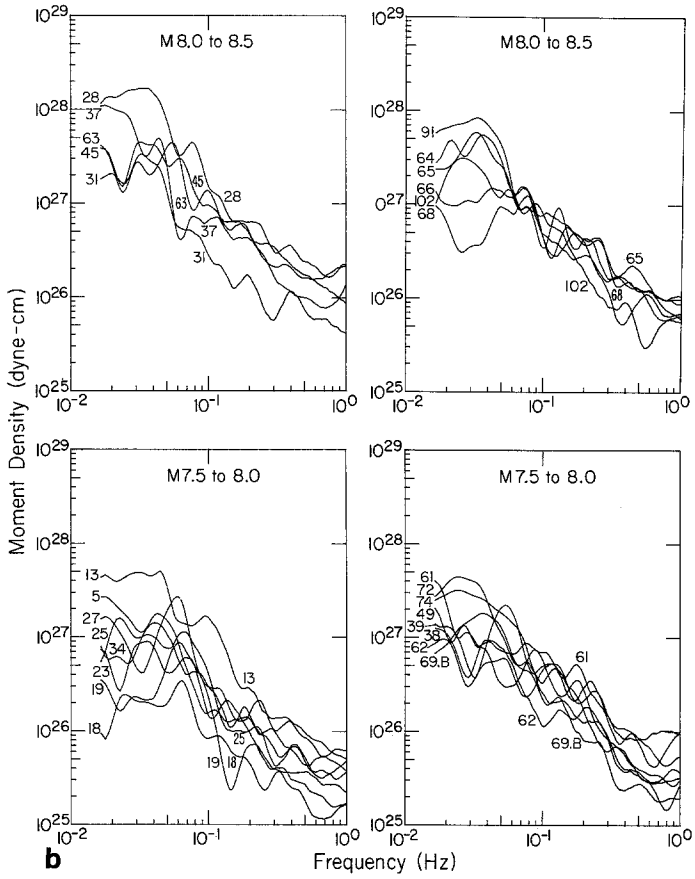

FIG. 11b

relatively coherently during an earthquake and are termed asperites. Lay *et al.* (1982) group subduction zones into four general categories with decreasing asperity size and decreasing coupling: (1) South Chile, Alaska, and Kamchatka; (2) Aleutians, Colombia, Nankai, and the Solomon Islands; (3) Kuriles, northeast Japan, Peru, and Central Chile; and (4) Marianas, Izu-Bonin, and Tonga.

In order to assess the results of this study in terms of the above asperity model and also to make the results more accessible for engineering purposes, the time functions have been characterized using five parameters. These parameters are: (1) spectral slope between 2 and 50 sec; (2) roughness; (3) multiplicity; (4) pulse widths; and (5) overall signal duration. Table 3 lists the values of these parameters for the major subduction zones. The values are based on the largest earthquake, $M_{w_{(max)}}$, that each trench is assumed capable of supporting. For cases when the $M_{w_{(max)}}$

earthquake did not occur during the time period for which there are 1–90 records, the largest event that did occur is used. The magnitude of this smaller earthquake is given in parentheses as are its time function parameters. For uniformity, the Wood-Anderson record that was deconvolved for the 1964 Alaska earthquake is not used in this tabluation, except for the measure of overall duration. Instead, a smaller event is chosen which has an on-scale 1–90 record. The values of spectral slope are taken from Table 2. The roughness parameter in Table 3 is a measure of the high-

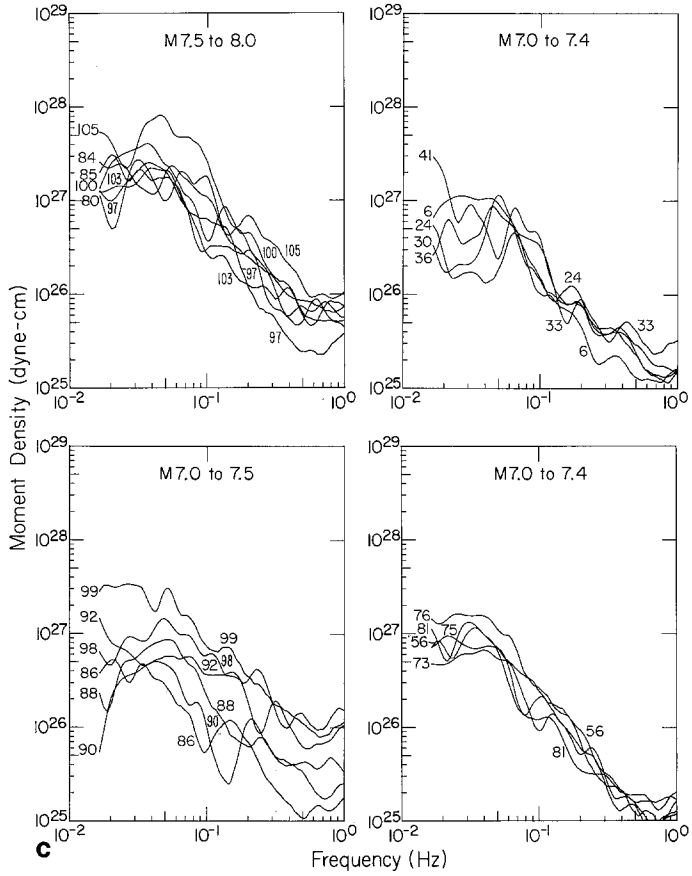

FIG. 11c

frequency content or sharpness of the time function. The roughness, R, is defined as

$$R = \frac{1}{n\nu}\left[a_1 + a_n + \sum_{i=2}^{n} |(a_i - a_{i-1})|\right], \tag{23}$$

where a_i is the moment in the ith time slice (0.9 sec in duration) of the time function, n is the total number of time slices, and ν is the average moment in the n time slices. The values of R in Table 3 have been normalized to vary between 0. and 1.0. A large value of $R(\sim 1.0)$ indicates a rapidly varying or sharp time function and a higher frequency time domain record. A small value of $R(\sim 0.0)$ indicates a smooth, broad time function and a predominantly longer period time domain record. To avoid inconsistent measurements due to the interference effect discussed earlier

between adjacent time slices in the discretized time function, all time functions are low-pass filtered with a corner at 0.4 Hz (2.5 sec) before computing the value of R. The multiplicity in Table 3 is the number of obvious discrete sources composing the earthquake. The pulse width is the average duration in seconds of each individual source. The overall duration is the duration in seconds of significant body-wave amplitude on the Pasadena 1–90 record.

Although the time function characteristics in Table 3 are based on the one or two largest events from each subduction zone, there may be considerable variations within a given subduction zone. The regions in Table 3 are arranged in order of decreasing $M_{w(\max)}$. The column (rate × 10)/age is included as a measure of coupling, following the conclusions of Uyeda and Kanamori (1979) and Ruff and Kanamori (1980) that coupling of the subducted plate should increase with decreasing age and

TABLE 3

CHARACTERISTICS OF TIME FUNCTIONS

Trench	$M_{w(\max)}$	Age (m.y.)	Convergence Rate (cm/yr)	Rate × 10 / Age	Spectral Slope	Roughness	Multiplicity	Pulse Width (sec)	Overall Duration (sec)
South Chile	9.5	20	11.1	5.55	−2.0	0.46	7	30	360
Alaska	9.2 (8.2)	40	5.9	1.47	−1.3*	0.92*	4*	35*	240†
Aleutians	9.1	60	7.5	1.25	−1.4	1.0	3	43	225
Kamchatka	9.0	80	9.3	1.16	−1.7	0.61	5	30	260
Colombia	8.8 (8.2)	20	7.7	3.85	−1.7*	0.92*	4*	25*	200*
Central Chile	8.5 (8.3 M_S)	50	11.0	2.20	−1.7*	0.38*	1*	25*	100*
Kuriles	8.5	100	9.3	0.93	−1.3	0.61	7	20	200
Nankai	8.4 (8.1)	20	3.5	1.75	−1.2*	1.0*	4*	25*	225*
Peru	8.2	45	10.0	2.22	−1.3	0.23	2	25	150
Solomon Islands	8.2 (8.1)	?	?	?	−1.3*	0.04*	1*	40*	150*
North and Central Honshu	8.2	130	9.7	0.75	−1.7	0.77	3	30	200
Tonga-Kermadec	8.2 (8.0 M_S)	120	7.6	0.63	−1.5*	0.46*	2*	25*	150*
Central America	8.1 (7.7 M_S)	45	8.0	1.77	−1.4*	0.84*	1*	15*	100*
New Hebrides	7.9 (7.5 M_S)	60	2.7	0.45	−1.8*	0*	1*	20*	100*

* For magnitude $< M_{w(\max)}$.

† Wood-Anderson record for 1964 Alaska.

increasing convergence rate. The plate ages and convergence rates are from Ruff and Kanamori (1980). In general, the multiplicity and the overall duration increase with increasing $M_{w(\max)}$. There does not appear to be a simple relationship between the roughness measure of the time function and $M_{w(\max)}$ or plate coupling. However, there is less variation of this parameter within a given region than between regions. Other factors such as plate boundaries or topographic features on the subducted plate may play a role. Some general observations, however, can be made. The time functions for earthquakes from Central Chile, Peru, Solomon Islands, and New Hebrides are simple and smooth. Solomon Islands earthquakes in particular are characterized by unusually broad, simple time functions. Alaska, Aleutians, Colombia, and Nankai produce earthquakes whose time functions are generally complex and rough. South Chile should perhaps be included in this group also, although its time function is somewhat smoother. It should be kept in mind that the roughness measure used here is for the period range of 2.5 to about 60 sec. As Figure 8 shows,

the time functions of the largest earthquakes can be very smooth at longer periods. Kamchatka and the Kuriles have unusually large multiplicities for the size of the earthquakes. The possibility of a water multiple was suggested earlier. However, with this interpretation, it is difficult to explain why water multiples are not seen for all the trenches. An alternative explanation is a very regular asperity interval. Both Kamchatka and the Kuriles also have low values of (rate × 10)/age for their respective $M_{w_{(\max)}}$, which may be related. There is no obvious relationship between the spectral slope from 2 to 50 sec and the value of $M_{w_{(\max)}}$ or time function roughness. This parameter may be a stronger function of the rupture geometry, which could vary significantly from event to event.

From studying the time functions for several large earthquakes, Ruff and Kanamori (1983) reasoned that asperity size increases with increasing magnitude. This conclusion is based primarily on the very broad (~120-sec duration), simple time function obtained for the 1964 Alaska earthquake compared with earthquakes in the Aleutians and Kuriles. The 1–90 data in this study are not of long enough period to resolve the complete time function of the Alaska earthquake. However, for smaller events, quite similar results are obtained as with WWSSN data (Figure 9). For these earthquakes, a larger asperity size for larger $M_{w_{(\max)}}$ does not always seem to be the rule. The Aleutians, Kamchatka, and the Kuriles seem to generate large earthquakes by a cascading rupture of several smaller asperities.

The results in Table 3 can be summarized by categorizing the subduction zones according to the characteristics of the earthquake time functions (multiplicity or complexity and roughness) as follows: (1) South Chile and Alaska; (2) Aleutians, Kamchatka, Kuriles, Colombia, and Nankai; (3) Northeast Japan, Tonga-Kermadec, and Central America; and (4) Central Chile, Peru, the Solomon Islands, and the New Hebrides. The aforementioned grouping is in order of decreasing multiplicity and roughness, not necessarily earthquake size. Group 2 is the most complex, and group 4 is the simplest and smoothest. Group 1 is a special group for regions with apparently significantly larger asperities. Alaska is included in this group based on the work of Ruff and Kanamori (1983) on the 1964 Alaska earthquake. Similar long-period analysis of the 1960 Chile earthquake is not available, and its placement in group 1 is tentative.

At the outset of this study, it was envisioned that the character of the teleseismic source time functions may vary in a systematic way with the variables, age of the subducted lithosphere, and convergence rate. If there are global trends of this nature, they are not obvious from the analysis of the 1–90 records. Nevertheless, some of the subduction zones do behave in very characteristic fashions. The smooth, simple time functions of Central Chile, Peru, the Solomon Islands, and the New Hebrides, the regular multiple event interval of Kamchatka and the Kuriles, and the long, complicated ruptures of the Aleutians, Colombia, and Nankai are the most prominent examples.

ACKNOWLEDGMENTS

This research was supported by the U.S. Nuclear Regulatory Commission. The authors benefited from discussions with Hiroo Kanamori, Larry Ruff, and Heidi Houston. The paper was significantly improved by reviews from Paul Spudich, Larry Ruff, and Dave Boore. We thank Masayuki Kikuchi and Larry Ruff for generously providing unpublished results. The 1–90 seismograms were patiently digitized by Bette Sheppard.

REFERENCES

Abe, K. (1972). Mechanisms and tectonic implications of the 1966 and 1970 Peru earthquakes, *Phys. Earth Planet. Interiors* **5**, 367–379.

Abe, K. (1973). Tsunami and mechanism of great earthquakes, *Phys. Earth Planet. Interiors* **7,** 143–153.

Abe, K. (1977). Tectonic implications of the large Shioya-Oki earthquakes of 1938, *Tectonophysics* **41,** 269–289.

Aki, K. (1983). Strong-motion seismology, in *Proceedings of the International School of Physics, Enrico Fermi, Earthquakes: Observation, Theory and Interpretation,* H. Kanamori and E. Boschi, Editors, North-Holland Publishing Co., New York, 223–245.

Beck, S. and L. Ruff (1984). The rupture process of the great 1979 Colombia earthquake: evidence for the asperity model, *J. Geophys. Res.* **89,** 9281–9191.

Boatwright, J. (1980). Preliminary body-wave analysis of the St. Elias, Alaska, earthquake of February 28, 1979, *Bull. Seism. Soc. Am.* **70,** 419–436.

Boore, D. and J. Boatwright (1984). Average body-wave radiation coefficients, *Bull. Seism. Soc. Am.* **74,** 1615–1621.

Bracewell, R. (1965). *The Fourier Transform and Its Applications,* McGraw-Hill Book Co., New York.

Bullen, K. E. (1963). *An Introduction to the Theory of Seismology,* Cambridge University Press, London, England.

Burdick, L. J. and G. Mellman (1976). Inversion of the body waves from the Borrego Mountain earthquake to the source mechanism, *Bull. Seism. Soc. Am.* **66,** 1485–1499.

Carpenter, E. W. (1966). Absorption of elastic waves—An operator for a constant Q mechanism, Atomic Weapons Research Establishment, Report 0-4366, Her Majesty's Station Office, London, England.

Chael, E. and G. Stewart (1982). Recent large earthquakes along the Middle American Trench and their implications for the subduction process, *J. Geophys. Res.* **87,** 329–338.

Chung, W.-Y. and H. Kanamori (1976). Source process and tectonic implications of the Spanish deep-focus earthquake of March 29, 1954, *Phys. Earth Planet. Interiors* **13,** 85–96.

Cormier, V. (1975). Tectonics near the junction of the Aleutian and Kuril-Kamchatka Arcs and a mechanism for middle Tertiary magmatism in the Kamchatka Basin, *Geol. Soc Am. Bull.* **86,** 443–453.

Davies, J., L. Sykes, L. House, and K. Jacob (1981). Shumagin seismic gap, Alaska Peninsula: history of great earthquakes, tectonic setting, and evidence for high seismic potential, *J. Geophys. Res.* **86,** 3821–3855.

Ebel, J. (1980). Source processes of the 1965 New Hebrides Islands earthquakes inferred from teleseismic waveforms, *Geophys. J. R. Astr. Soc.* **63,** 381–403.

Fukao, Y. (1979). Tsunami earthquakes and subduction processes near deep-sea trenches, *J. Geophys. Res.* **84,** 2303–2314.

Fukao, Y. and M. Furumoto (1979). Stress drops, wave spectra and recurrence intervals of great earthquakes—Implications of the Etorofu earthquake of 1958 November 6, *Geophys. J. R. Astr. Soc.* **57,** 23–40.

Futterman, W. I. (1962). Dispersive body waves, *J. Geophys. Res.* **67,** 5279–5291.

Gusev, A. A. (1983). Decriptive statistical model of earthquake source radiation and its application to an estimation of short-period strong motion, *Geophys. J. R. Astr. Soc.* **74,** 787–808.

Hartzell, S. and T. Heaton (1983). Inversion of strong ground motion and teleseismic waveform data for the fault rupture history of the 1979 Imperial Valley, California, earthquake, *Bull. Seism. Soc. Am.* **73,** 1553–1583.

Haskell, N. (1966). Total energy and energy spectral density of elastic wave radiation from propagating faults. Part II. A statistical source model, *Bull. Seism. Soc. Am.* **56,** 125–140.

Heaton, T. (1982). The 1971 San Fernando earthquake: a double event? *Bull. Seism. Soc. Am.* **72,** 2037–2062.

Helmberger, D. (1983). Theory and application of synthetic seismograms, in *Proceedings of the International School of Physics, Enrico Fermi, Earthquakes: Observation, Theory and Interpretation,* H. Kanamori and E. Boschi, Editors, North-Holland Publishing Co., New York, 174–222.

Ichikawa, M. (1971). Reanalyses of mechanism of earthquakes which occurred in and near Japan, and statistical studies on the nodal plane solutions obtained, 1926–1968, *Geophys. Mag.* **35,** 207–274.

Isacks, B., L. Sykes, and J. Oliver (1969). Focal mechanisms of deep and shallow earthquakes in the Tonga-Kermadec region and the tectonics of island arcs, *Geol. Soc. Am. Bull.* **80,** 1443–1470.

Kanamori, H. (1970a). Synthesis of long-period surface waves and its application to earthquake sources studies—Kurile Islands earthquake of October 13, 1963, *J. Geophys. Res.* **75,** 5011–5027.

Kanamori, H. (1970b). The Alaska earthquake of 1964: radiation of long-period surface waves and source mechanism, *J. Geophys. Res.* **75,** 5029–5040.

Kanamori, H. (1971). Focal mechanism of Tokachi-Oki earthquake of May 16, 1968, *Tectonophysics* **12,** 1–13.

Kanamori, H. (1972a). Tectonic implications of the 1944 Tonankai and the 1946 Nankaido earthquakes, *Phys. Earth Planet. Interiors* **5,** 129–139.

Kanamori, H. (1972b). Mechanism of tsunami earthquakes, *Phys. Earth Planet. Interiors* **6**, 346–359.

Kanamori, H. (1976). Re-examination of the earth's free oscillations excited by the Kamchatka earthquake of November 4, 1952, *Phys. Earth Planet. Interiors* **11**, 216–226.

Kanamori, H. and J. Cipar (1974). Focal process of the great Chilean earthquake May 22, 1960, *Phys. Earth Planet. Interiors* **9**, 128–136.

Kanamori, H. and G. Stewart (1978). Seismological aspects of the Guatemala earthquake of February 4, 1976, *J. Geophys. Res.* **83**, 3427–3434.

Kanamori, H. and J. W. Given (1981). Use of long-period surface waves for fast determination of earthquake source parameters, *Phys. Earth Planet. Interiors* **27**, 8–31.

Kanamori, H. and L. Astiz (1984). The 1983 Akita-Oki earthquake (M_w = 7.8) and its implications for systematics of subduction earthquakes, *Earthquake Pred. Res.* (in press).

Kasahara, M. (1975). Fault model of the 1952 Tokachi-Oki earthquakes, *Abstr. Ann. Meeting Seism. Soc. Japan* **2**, 90.

Katsumata, M. and L. Sykes (1969). Seismicity and tectonics of the western Pacific: Izu-Mariana-Caroline and Ryukyu-Taiwan Regions, *J. Geophys. Res.* **74**, 5923–5948.

Kelleher, J., L. Sykes, and J. Oliver (1973). Possible criteria for predicting earthquake locations and their application to major plate boundaries of the Pacific and the Caribbean, *J. Geophys. Res.* **78**, 2547–2585.

Kikuchi, M. and H. Kanamori (1982). Inversion of complex body waves, *Bull. Seism. Soc. Am.* **72**, 491–506.

Kikuchi, M. and Y. Fukao (1984). Iterative deconvolution of complex body waves from great earthquakes—The Tokachi-Oki earthquake of 1968 (submitted for publication).

Lay, T. and H. Kanamori (1980). Earthquake doublets in the Solomon Islands, *Phys. Earth Planet. Interiors* **21**, 283–304.

Lay, T., H. Kanamori, and L. Ruff (1982). The asperity model and the nature of large subduction zone earthquakes, *Earthquake Pred. Res.* **1**, 3–71.

Lawson, C. L. and R. J. Hanson (1974). *Solving Least Squares Problems*, Prentice-Hall, Inc., Englewood Cliffs, New Jersey.

Malgrange, M., A. Deschamps, and R. Madariaga (1981). Thrust and extensional faulting under the Chilean coast: 1965, 1971 Aconcagua earthquakes, *Geophys. J. R. Astr. Soc.* **66**, 313–331.

McNally, K. and J. B. Minster (1981). Nonuniform seismic slip rates along the Middle America Trench, *J. Geophys. Res.* **86**, 4949–4959.

Mikumo, T. (1971). Source process of deep and intermediate earthquakes as inferred from long-period *P* and *S* waveforms, *J. Phys. Earth* **19**, 1–20.

Mori, A. W. and C. B. Crouse (1981). Strong motion data from Japanese earthquakes, World Data Center A for Solid Earth Geophysics, NOAA, Report SE-29.

Nabelek, J. (1984a). Determination of earthquake source parameters from inversion of body waves, *Ph.D. Thesis*, Massachusetts Institute of Techology, Cambridge, Massachusetts.

Nabelek, J. (1984b). A procedure for determination of spacial and temporal history of faulting from inversion of teleseismic body waves: application to the September 6, 1975 Lice, Turkey earthquake (submitted for publication).

Oppenheim, A. and R. Schafer (1975). *Digital Signal Processing*, Prentice-Hall, Englewood Cliffs, New Jersey.

Regan, J. and H. Kanamori (1980). A complex earthquake sequence in the Kurile Islands (March 23, 24, 1978): its implications on the behavior of seismic gaps (abstract), *Trans. Am. Geophys. Union, EOS* **61**, 1026.

Ruff, L. and H. Kanamori (1980). Seismicity and the subduction process, *Phys. Earth Planet. Interiors* **23**, 240–252.

Ruff, L. and H. Kanamori (1983). The rupture process and asperity distribution of three great earthquakes from long-period diffracted *P*-waves, *Phys. Earth Planet. Interiors* **31**, 202–230.

Schwartz, S. and L. Ruff (1985). The rupture process of the 1968 Tockachi-Oki and the 1969 Kurile Islands earthquakes: support for the asperity model of large earthquake occurrence, *J. Geophys. Res.* (in press).

Seno, T. and T. Eguchi (1983). Seismotectonics of the western Pacific region (submitted for publication).

Seno, T., K. Shimazaki, P. Somerville, K. Sudo, and T. Eguchi (1980). Rupture process of the Miyagi-Oki, Japan, earthquake of June 12, 1978, *Phys. Earth Planet. Interiors* **23**, 39–61.

Shimazaki, K. (1974). Nemuro-Oki earthquake of June 17, 1973: a lithospheric rebound at the upper half of the interface, *Phys. Earth Planet. Interiors* **9**, 314–327.

Shiono, K., T. Mikumo, and Y. Ishikawa (1980). Tectonics of the Kyushu-Ryukyu arc as evidenced from seismicity and focal mechanism of shallow to intermediate-depth earthquakes, *J. Phys. Earth* **28**, 17–43.

Stauder, W. (1973). Mechanism and spatial distribution of Chilean earthquakes with relation to subduction of the oceanic plate, *J. Geophys. Res.* **78,** 5033–5061.

Stewart, G. and H. Kanamori (1982). Complexity of rupture in large strike-slip earthquakes in Turkey, *Phys. Earth Planet. Interiors* **28,** 70–84.

Sykes, L. (1971). Aftershock zones of great earthquakes, seismicity gaps, and earthquake prediction for Alaska and the Aleutians, *J. Geophys. Res.* **76,** 8021–8041.

Taber, J. (1983). Crustal structure and seismicity of the Washington continental margin, *Ph.D. Thesis,* University of Washington, Seattle, Washington.

Uyeda, S. and H. Kanamori (1979). Back-arc opening and the mode of subduction, *J. Geophys. Res.* **84,** 1049–1061.

Vidale, J. and H. Kanamori (1983). The October 1980 earthquake sequence near the New Hebrides, *Geophys. Res. Letters* **10,** 1137–1140.

Ward, S. (1979). Ringing *P* waves and submarine faulting, *J. Geophys. Res.* **84,** 3057–3062.

Wu, F. and H. Kanamori (1973). Source mechanism of February 4, 1965, Rat Island earthquake, *J. Geophys. Res.* **78,** 6082–6092.

Yoshioka, N. and K. Abe (1976). Focal mechanism of the Iwate-Oki earthquake of June 12, 1968, *J. Phys. Earth* **24,** 251–262.

UNITED STATES GEOLOGICAL SURVEY
SEISMOLOGY BRANCH
CALIFORNIA INSTITUTE OF TECHNOLOGY
PASADENA, CALIFORNIA 91125

Manuscript received 6 December 1985

APPENDIX

The Appendix consists of Figures A1 to A19.

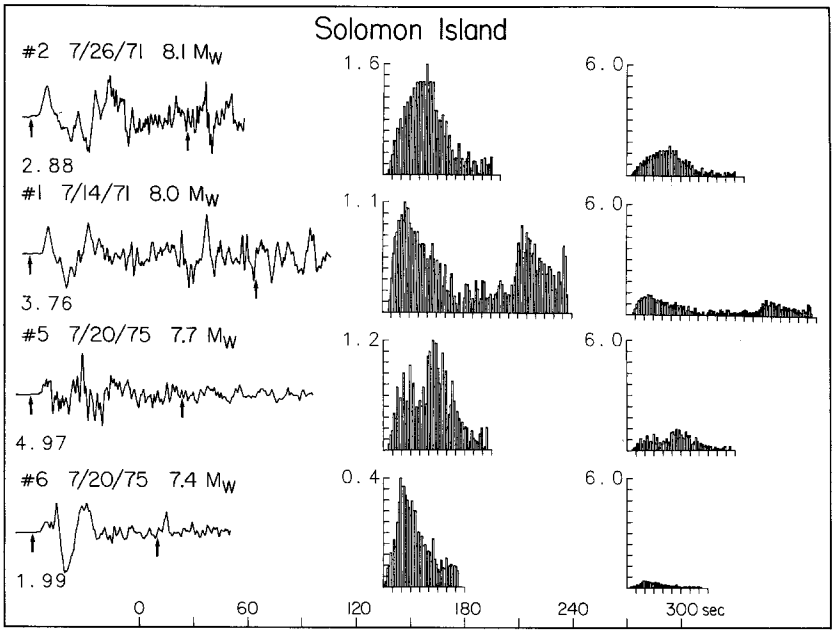

FIG. A1. Teleseismic source time functions obtained from the Pasadena Benioff 1–90 records. Each time function is plotted twice: once full-scale and second with a common full-scale amplitude. The 1–90 records are shown on the *left* with the peak record amplitude given in microns for unit gain. The pair of arrows under each record indicate the section of the *P* waveform used in the calculation of the time function. Vertical scales for the time functions are in units of 10^{26} dyne-cm.

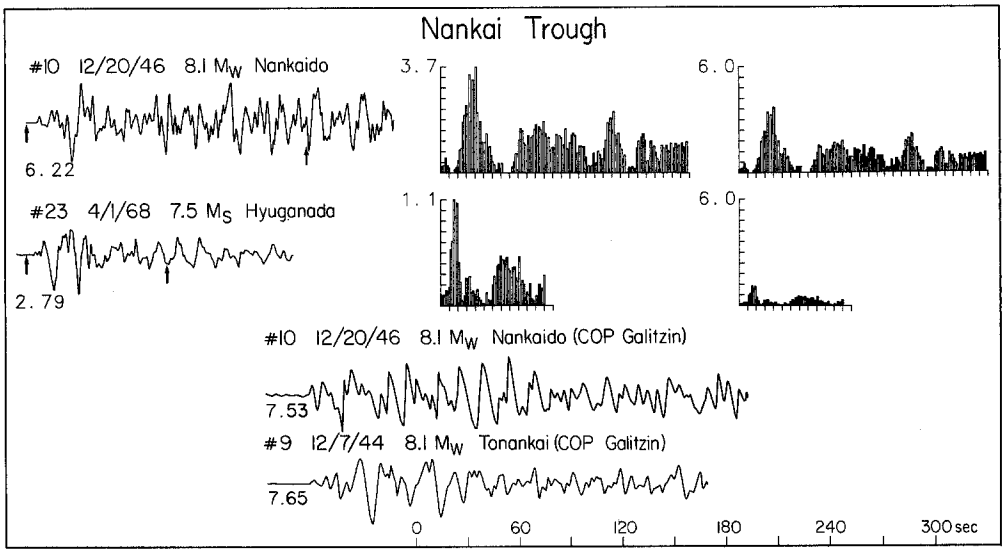

FIG. A2. Same as Figure A1.

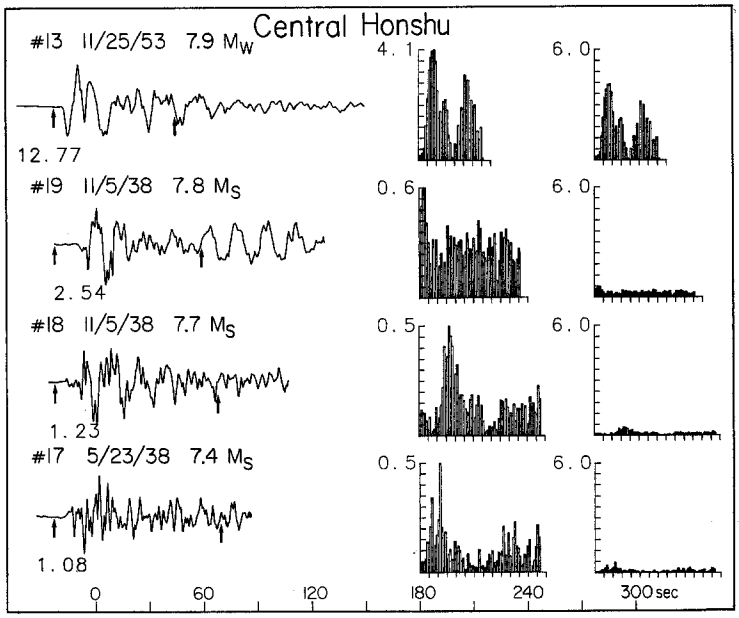

FIG. A3. Same as Figure A1.

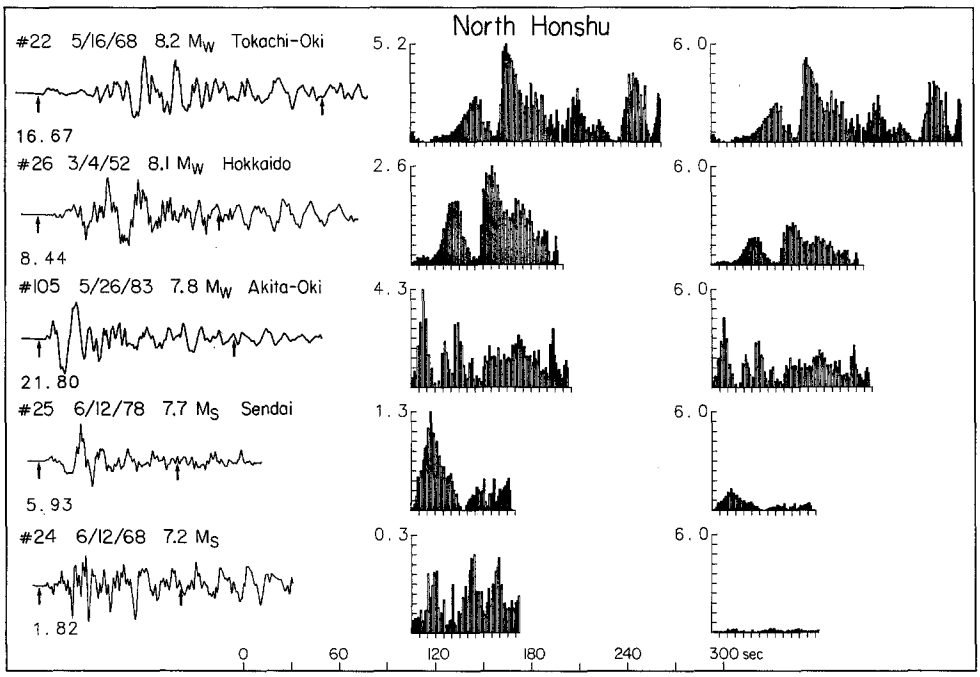

FIG. A4. Same as Figure A1.

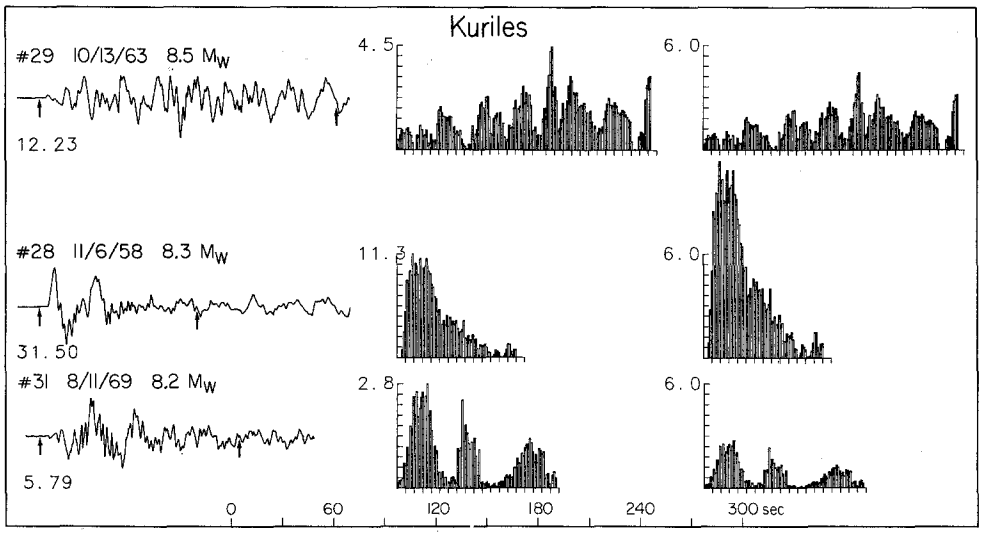

FIG. A5. Same as Figure A1.

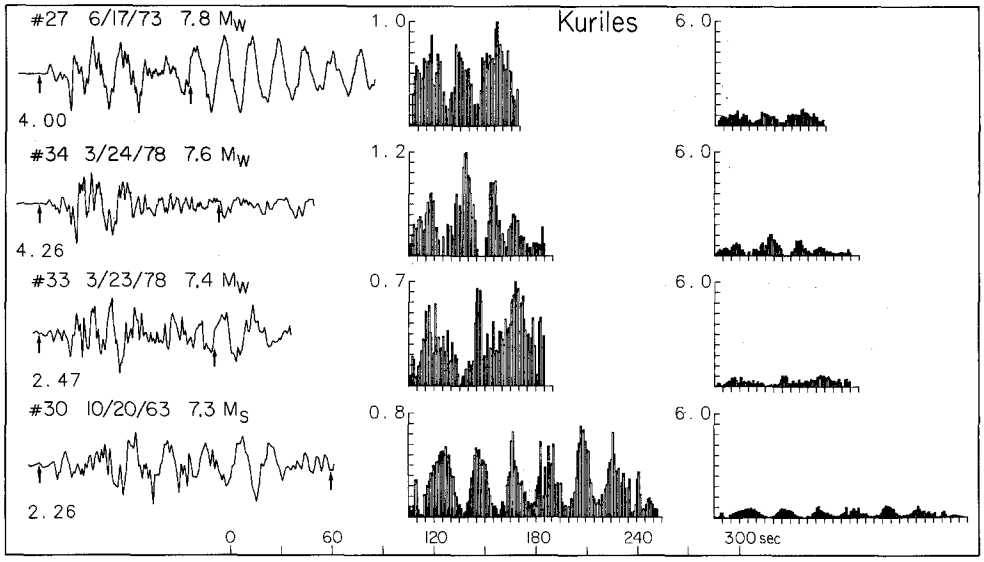

FIG. A6. Same as Figure A1.

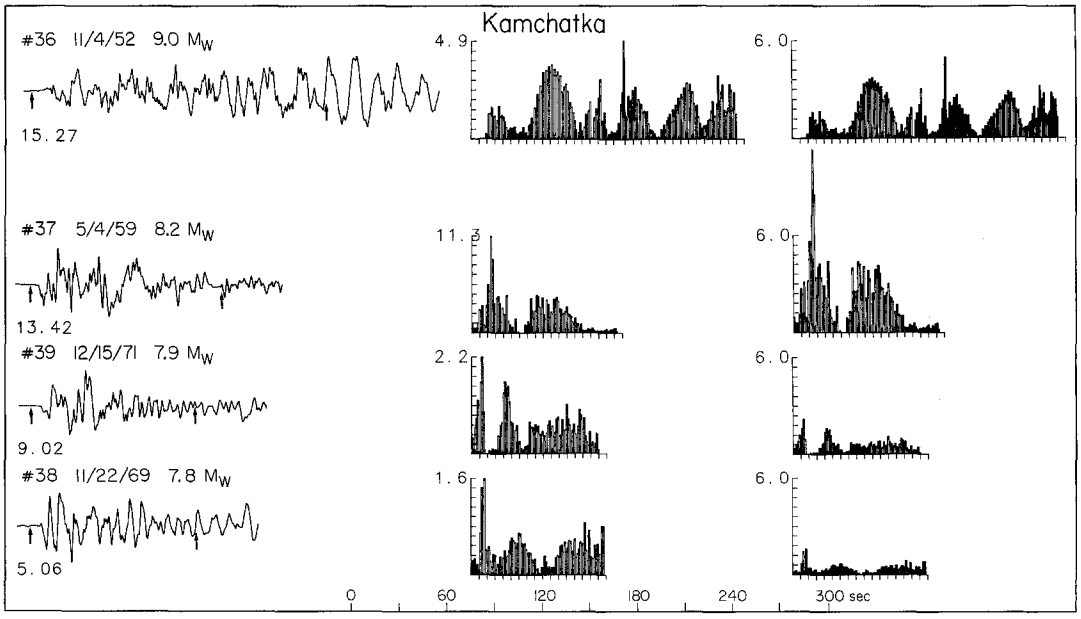

FIG. A7. Same as Figure A1.

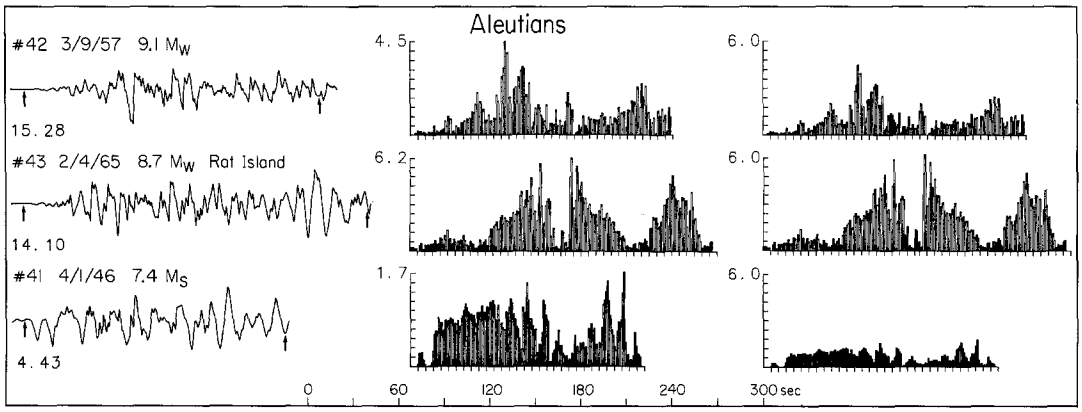

FIG. A8. Same as Figure A1.

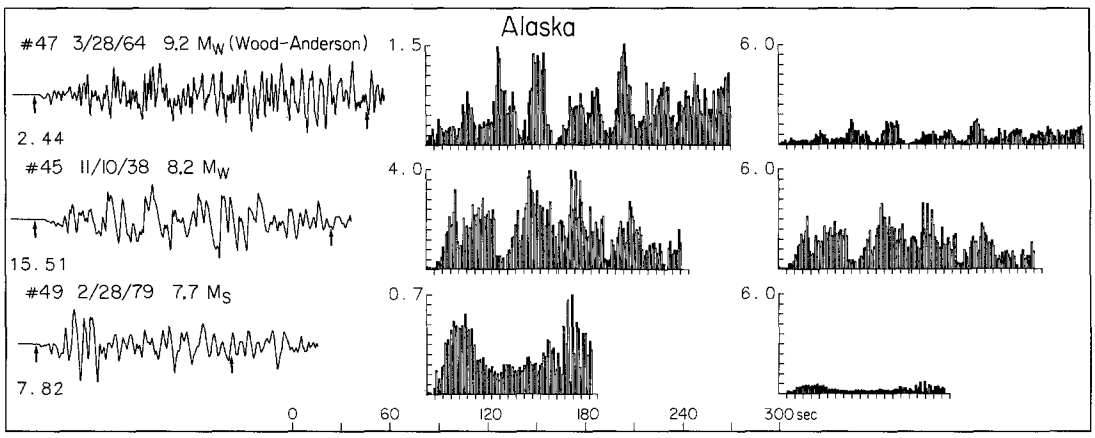

FIG. A9. Same as Figure A1.

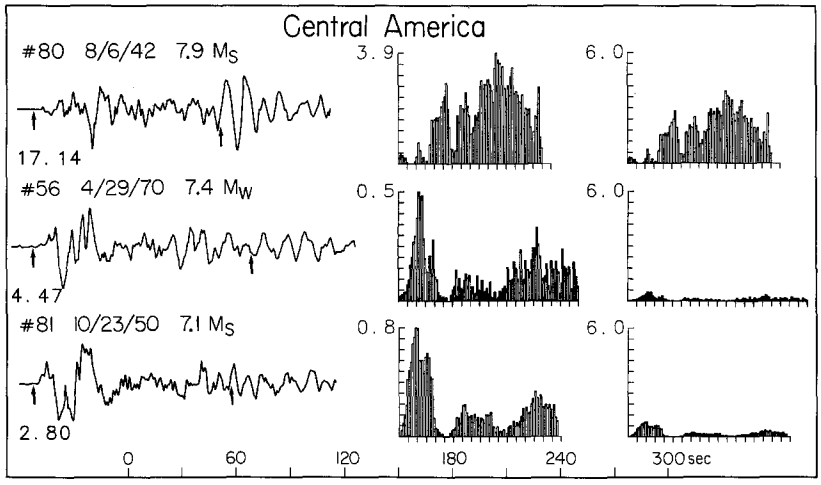

FIG. A10. Same as Figure A1.

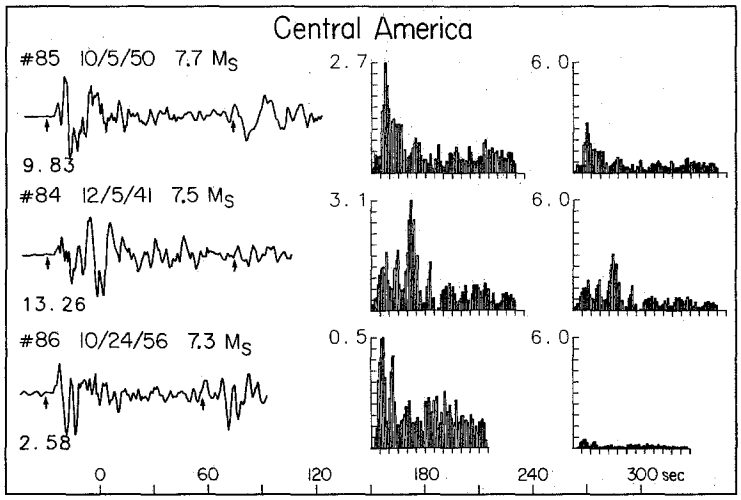

FIG. A11. Same as Figure A1.

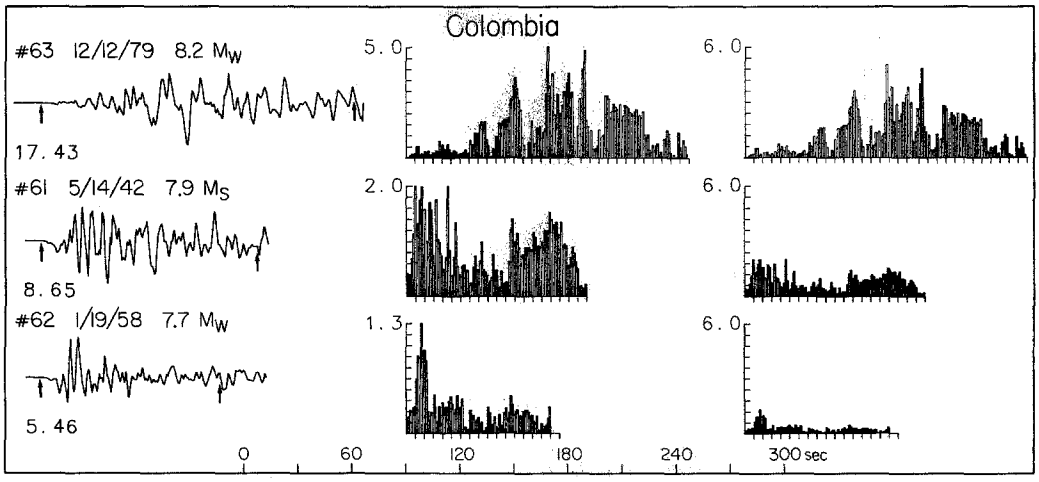

FIG. A12. Same as Figure A1.

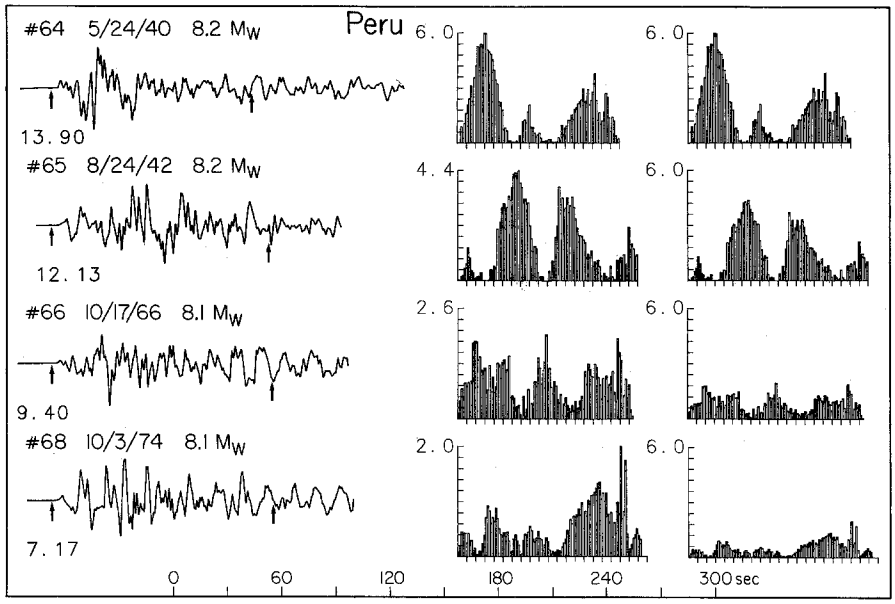

FIG. A13. Same as Figure A1.

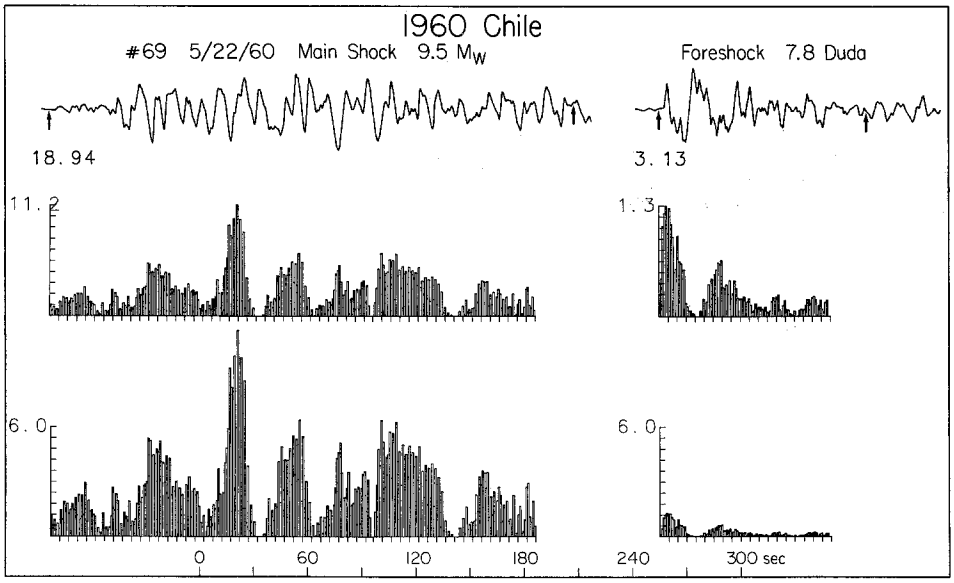

FIG. A14. Same as Figure A1.

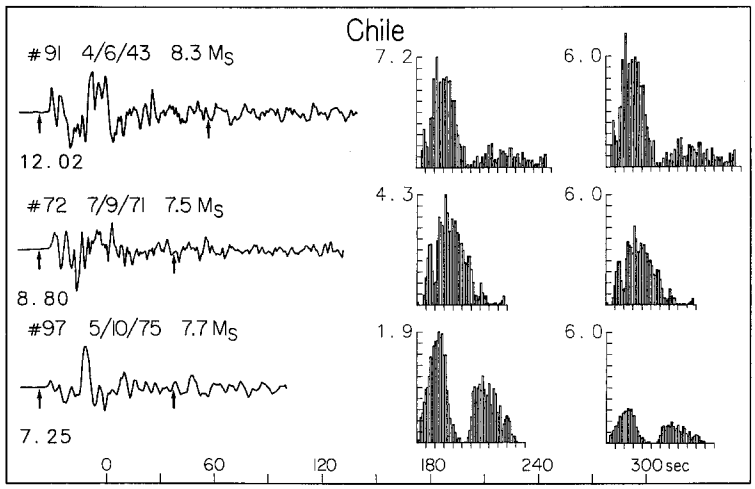

FIG. A15. Same as Figure A1.

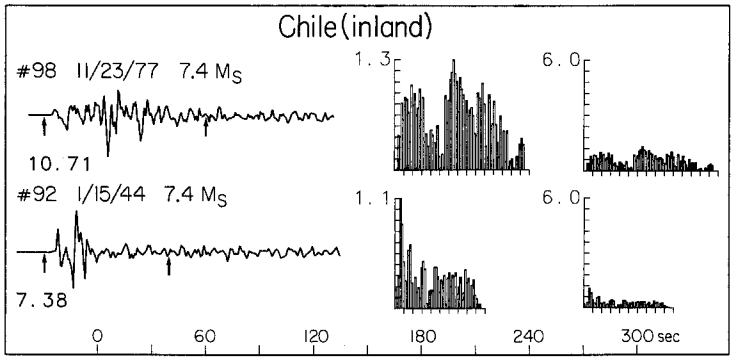

FIG. A16. Same as Figure A1.

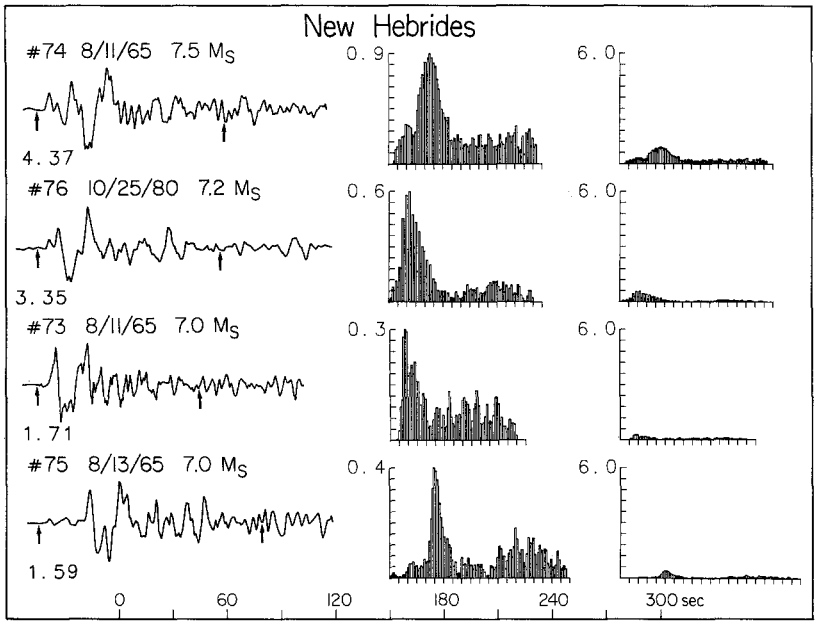

FIG. A17. Same as Figure A1.

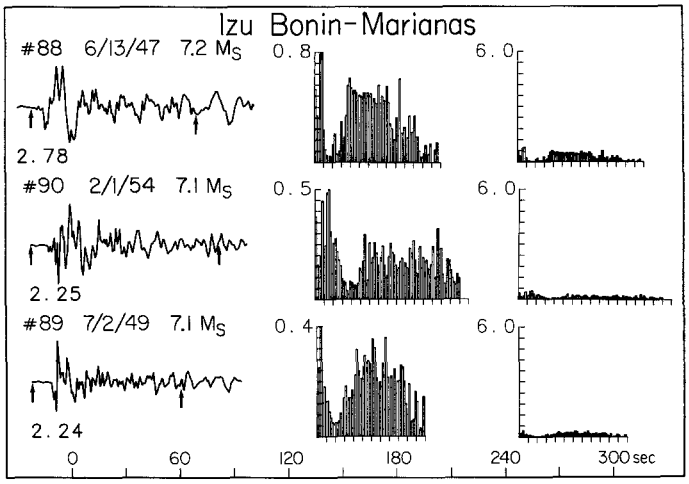

FIG. A18. Same as Figure A1.

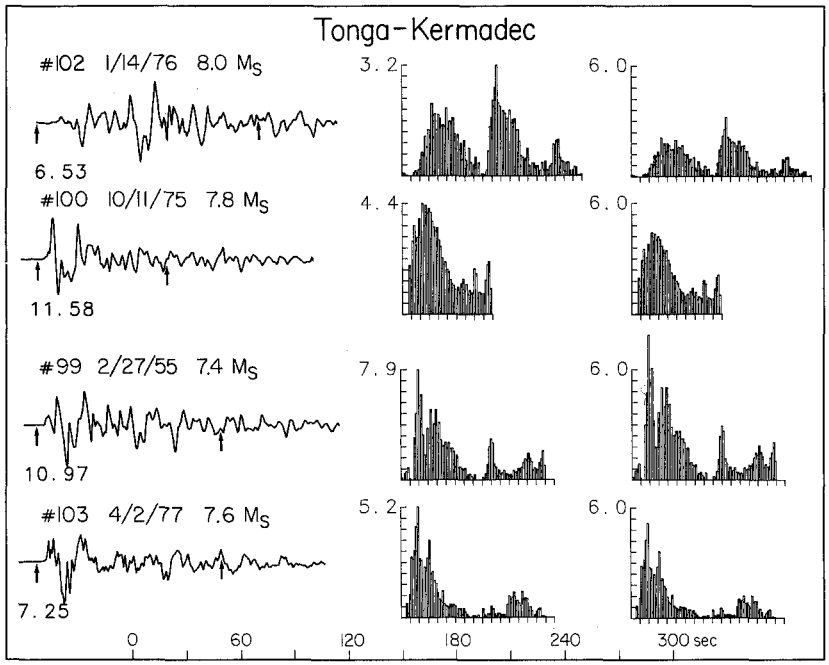

FIG. A19. Same as Figure A1.